5-2016

High Step-Up/Down Transformerless Multilevel Converter for Renewable Energy Applications

Haider Ghazi Mhiesan
University of Arkansas, Fayetteville

Citation

High Step-Up/Down Transformerless Multilevel Converter for Renewable Energy Applications

A thesis submitted in partial fulfillment
of the requirements for the degree of
Master of Science in Electrical Engineering

By

Haider Ghazi Mhiesan
University of Kufa
Bachelor of Science in Electrical Engineering, 2007

May 2016
University of Arkansas

This thesis is approved for recommendation to the Graduate Council.

_____

Dr. Roy McCann

Thesis Director

_____   _____

Dr. Simon Ang   Dr. Juan Carlos Balda

Committee Member   Committee Member

ABSTRACT

This thesis focuses on a high step-up/down transformerless dc-dc modular multilevel converter (MMC) that would be applicable to dc power systems. The design achieves high voltage ratios for interfacing renewable energy sources such as photovoltaic and line interactive Uninterruptible Power System (UPS) systems. The circuit topology provides for high step-up/down dc-dc conversion ratios using an MMC approach operating in resonant mode in order to improve overall efficiency. This topology operates to step-up the input voltage with 1:10 or larger conversion ratio. As a bidirectional converter, it also provides step-down capability at the same voltage ratio (10:1 or greater). The MMC circuit system consists of an upper and lower set of cells. The number of the upper cells is N, and the number of the lower cells is M. Phase-shift pulse width modulation (PS-PWM) is used to control voltage and power flow. PS-PWM with high duty cycle is generated to ensure that all the capacitors are connected except for one of them, which is out of the connection. A MATLAB/Simulink™ and LTspice simulations for the proposed topology are presented. Moreover, PV and UPS systems with the proposed topology are simulated using MATLAB/Simulink™. In photovoltaic application systems, a closed loop control system is represented for voltage regulation in case there is a change in the input voltage. In UPS application, closed loop controllers for charging and discharging batteries are presented.

ACKNOLEDGMENTS

I'd like to express my gratitude to Dr. McCann for helping me along this journey. To my committee, Dr. Ang and Dr. Balda, thank you for taking the time to be a part of my committee.

Tracey and Mr. Saunders, thank you for always being available to help me when I need it. To Kirsch Mackey, Clifford Kintner, Zachary Zelenka, and Kenny George who have helped me throughout the years whether it be helping to find resources or to help with my work, I thank you.

I could not find words to express my gratitude to Gloria Flores at the Graduate School and International Education for her support and help throughout my studies.

Last, but certainly not least, thank you to my entire family for always supporting me with everything that I do, especially my parents. I wouldn't be here if it wasn't for you all. Thank you.

TABLE OF CONTENTS

TABLE OF FIGURES

TABLE OF TABLES

CHAPTER ONE

INTRODUCTION

1.1 Brief History of Isolated and Non-isolated Converters

There has been a rapid development of photovoltaic solar cells and batteries for dc supplies and transmission lines. In addition to pollution problems, green energy related technologies have been increasing significantly due to the need for reducing carbon emissions. This in turn has encouraged many researchers, corporations and governments to increase the investigation of renewable energy. This has led to increased use of dc-microgrid systems that can supply the load from renewable energy to dc loads with improved levels of power quality [1]. The power from renewable energy can be used immediately to supply to the load, or it could be saved when there is a surplus for later availability such as at nighttime if using solar energy. In some cases renewable energy systems might have concerns for low voltage conditions. For instance, the battery energy storage system, supercapacitor, and photovoltaic generate low voltage levels as they become discharged and therefore cannot be connected directly to the dc-bus. Converters could be used to boost the voltage to fill the needs of the load or transmission line requirements. Due to these concerns, the development of high step-up/down converters has become one of the most important and significant solutions for adopting renewable energy [2, 3].

There are many types of converters that can achieve high step-up/down conversion ratios. Generally, high step-up/down converter can be classified into two being either isolated or non-isolated types.

There are many kinds of high step-up isolated converters that are used in microgrid applications. Phase-shifted full-bridge converters can operate under Zero Volte Switching (ZVS). For ZVS the main disadvantage is that the stress voltage on the output diode is higher than the output voltage. Also, these types of converters tend to have EMI problems due to increased input current ripple characteristics [4].

The dual current-fed boost converter divides the input current by using two inductors. This leads to the copper losses and inductor size being reduced. However, the main disadvantage of this type of converter is that the switches cannot operate under soft switching technique. That results in the dual current-fed boost converter being most suitable for low power applications [4].

A high voltage gain can be achieved by conventional boost, cascaded boost, switched capacitor, and switched inductor converters. These may have limitations due to diode reverse recovery currents resulting in reduced circuit reliability. Also, to have high step-up voltage there might be electromagnetic interface concerns due to the relatively high duty cycle levels [5]. In addition, there is a limitation when being used for high step-up voltage ratios because of the associated current spike may degrade component lifetime or induce a failure [6].

These problems can be solved by using other types of conventional isolated converters such as fly-back, forward, push-pull and single end primary inductor converters. That could be done by adjusting the turns-ratio. However, the switches have high voltage spikes that can be caused in the transformer by the leakage of inductance energy. In addition, a high turns-ratio increases the transformer size, losses, and cost. This results in reductions in the system efficiency [2], [5] and [7].

Dual output dc-dc boost can overcome the above problems, but its conversion ratio is generally low [5]. Secondary series and voltage lift can also produce a high voltage conversion ratio, but it needs more control complexity [7].

As is mentioned earlier, transformer converters can achieve a high step-up/down conversion ratio easily by adjusting the turns-ratio when the number of primary to secondary turns is large. However, there are several problems when the transformer has large number of turns ratio that can be summarized as the following points [6]:

- Large leakage inductance

- Parasitic capacitors that are created by the secondary winding of the transformer

- Spike that is caused by parasitic circuit effects

- Increased component heating losses

- Increased audible noise from inductor windings

- Large input filters are required

- Switching voltage transients are more pronounced

- Increased cost associated with the trabsformer

Many of the above problems can be eliminated by using transformerless converters. Transformerless power electronic energy converter systems can provide many advantages, such as being cost effective and with reduced size [8-10].

A transformerless converter is does not provide galvanic isolation. However, UL 1741 does allow for non-isolated converters if using more than one fuse to provide ground fault protection. A trip-time setting should be designed to make the non-isolated system capable of sensing short circuit conditions and deenergize the system in less than 0.040 seconds.

1.2 Thesis Motivation

The inclusion of dc elements in electric power grid is expanding rapidly because the adoption of solar photovoltaic energy and the capability of modern power electronics. Renewable energy systems that are connected to dc power systems require a high step-up/down conversion ratio converter. Most developments in converter topologies for connection renewable energy systems to dc power systems have been done for small and medium scale systems.

There are many challenges with connecting dc renewable energy systems to ac electric power systems:

- A small size and low-cost converter is needed in order to be effective compared to existing fossil fuel generation.

- Include balancing control for high step-up/down dc-dc ratios.

- Bidirectional energy conversion capability for incorporating battery energy storage with the renewable energy sources.

- Have improved efficiency and voltage regulation.

- Be able to provide a simple implementation for electrical interfaces.

1.3 Thesis Objectives

This thesis develops a topology that can work with many of the renewable energy systems. This topology provides a small, low-cost, direct, and simple solution for high step-up/down converters. This converter can operate with a simple control system. The absence of a transformer makes this circuit more cost-effective. The circuit that is developed provides a proof of concept for a medium voltage dc-dc modular multilevel converter [7] but with added

4

capability for bidirectional power conversion and protective features that have been developed to meet the requirements of UL 1741. It is shown how this converter compares to other medium-voltage dc-dc topologies and the effectiveness of the circuit during fault conditions. Moreover, the renewable energy sources such as energy storage and photovoltaic systems may cause instability of power grid because of reversed power flows. The circuit developed in this research is shown to also act as a voltage regulator to minimize this destabilizing effect.

1.4 Thesis Organization

To achieve the main objective of this thesis, chapters are written as the following:

- Chapter 2 presents the transformerless modular multilevel converter configuration and operating principles.

- Chapter 3 presents analytical and simulation results using MATLAB-Simulink and LTspice.

- Chapter 4 presents experimental results for a gate driver using a SiC MOSFET.

- Chapter 5 explains the applications and advantages of a transformerless modular multilevel converter.

- Chapter 6 develops an application of the converter as an Uninterruptible Power System (UPS).

- Chapter 7 presents the conclusions and recommendations for future work.

CHAPTER TWO

A HIGH STEP-UP/DOWN TRANSFOMERLESS MODULAR MULTILEVEL

CONVERTER MMC

2.1   Introduction

Researchers have been working to improve multilevel converters such that they are now used in many commercial products [11]. Different types of multilevel converters have been introduced. In order to achieve increased operating voltages, the modular multilevel converter (MMC) has been investigated [11]-[18]. This chapter develops a transformerless MMC configuration as a new development beyond was has previously been developed in [19] and [20].

2.2   A high step-up/down transformerless MMC

The circuit topology is a technology for high step-up dc-dc conversion ratio using the MMC approach operating in resonant mode in order to improve overall efficiency. The system has upper and lower cells. The low side inductor L is used to maintain the input source voltage. Fig. 2.1 shows the high step-up topology [20]. In this work the number of the upper cells is $N=4$ and the number of the lower cells is $M=2$ as shown in Fig. 2.2. Phase-shift pulse width modulation (PS-PWM) is used in this topology. PS-PWM with high duty cycle is generated to ensure one of the following conditions:

1) At least three of the upper capacitors are connected in series with any one of the lower capacitors.

2) Only the four upper capacitors are connected in series.
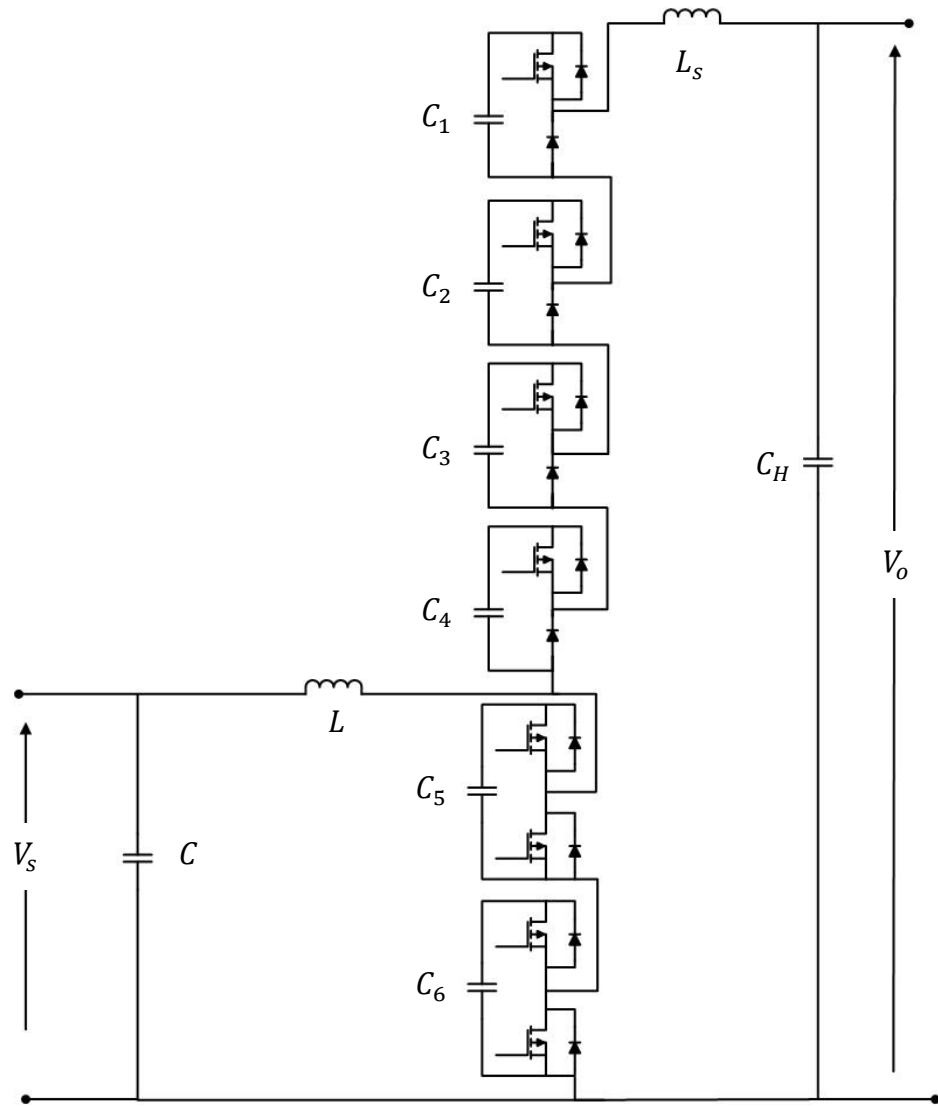
Fig. 2.1. A high step-up transformerless modular multilevel converter [20]
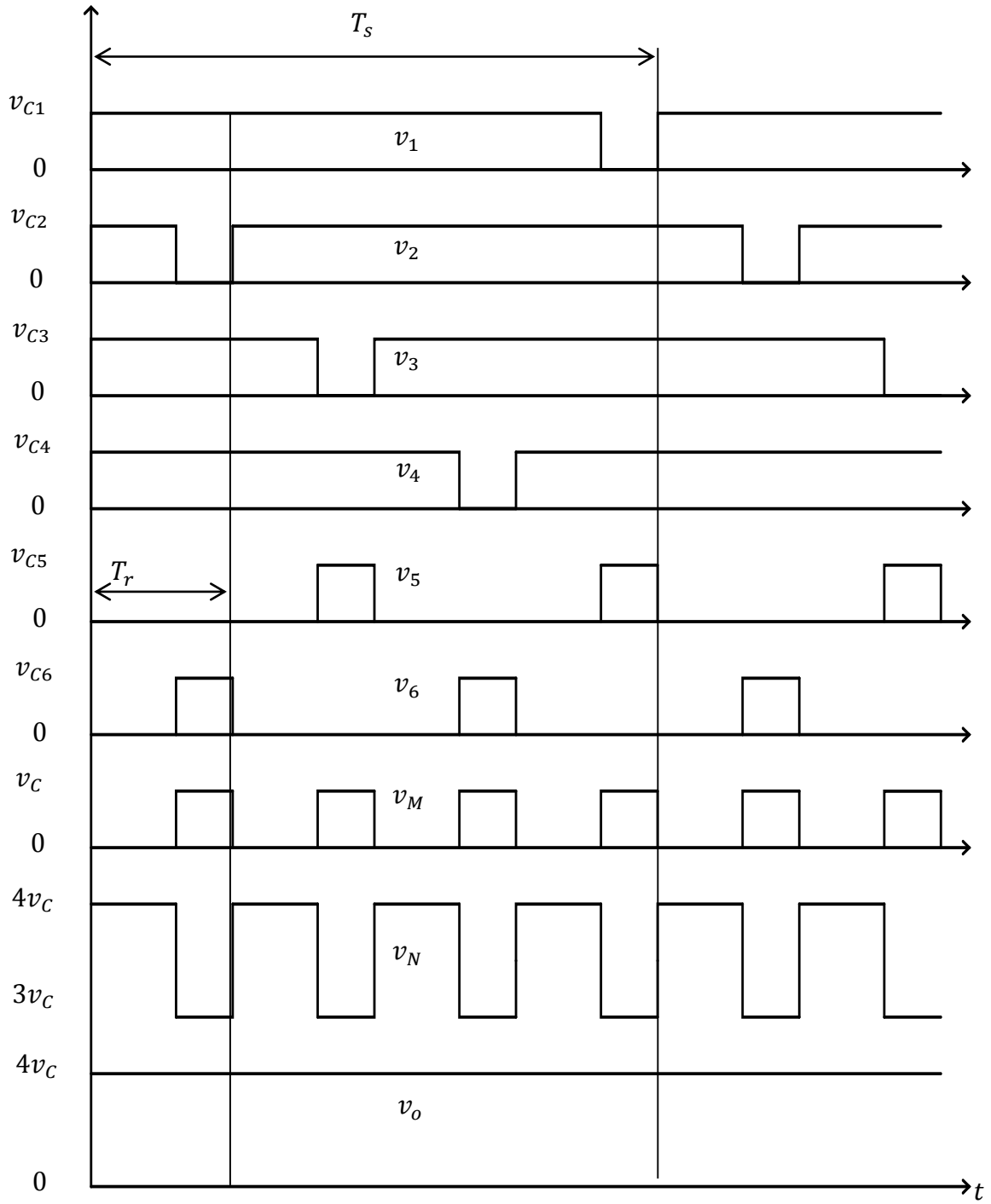
Fig. 2.2 Waveforms of the submodule and output voltage of the high step-up converter.

8

2.3. Operation modes configurations

In this topology there are eight modes as shown in Fig. 2.2, where it is shown that the upper and lower voltages are complementary. Also the operation frequency is four times the frequency of the lower cells. The operating switching frequency T_e is indicated for these eight modes and is defined in Table I.

2.3.1 Modes 1, 3, 5, and 7

From Table I, it is clear that modes 1, 3, 5, and 7 are the same. During these modes, all of the upper submodule capacitors are connected to the resonant inductor, thereby creating a resonant tank as indicated in Fig. 2.3(a). The output voltage is the sum of the capacitor voltages of the upper submodules. Therefore, the output voltage for modes 1, 3, 5, and 7 can be written as:

$$v_o = v_{c1} + v_{c2} + v_{c3} + v_{c4} , \qquad (2.1)$$

Table 2.1. Modes configaration during one period

	Mode 1	Mode 2	Mode 3	Mode 4	Mode 5	Mode 6	Mode 7	Mode 8
v_{c1}	v_c	v_c	v_c	v_c	v_c	v_c	v_c	0
v_{c2}	v_c	0	v_c	v_c	v_c	v_c	v_c	v_c
v_{c3}	v_c	v_c	v_c	0	v_c	v_c	v_c	v_c
v_{c4}	v_c	v_c	v_c	v_c	v_c	0	v_c	v_c
v_{c5}	0	0	0	v_c	0	0	0	v_c
v_{c6}	0	v_c	0	0	0	v_c	0	0

9

where v_o is the output voltage, and v_{c1}, v_{c2}, v_{c3}, and v_{c4} are the capacitor voltages for submodules 1 through 4, respectively. It should be noted that the output voltages during modes 1, 3, 5, and 7 are the same as v_o. In steady state, the capacitor's voltages are assumed to be equal. Therefore; the output voltage is:
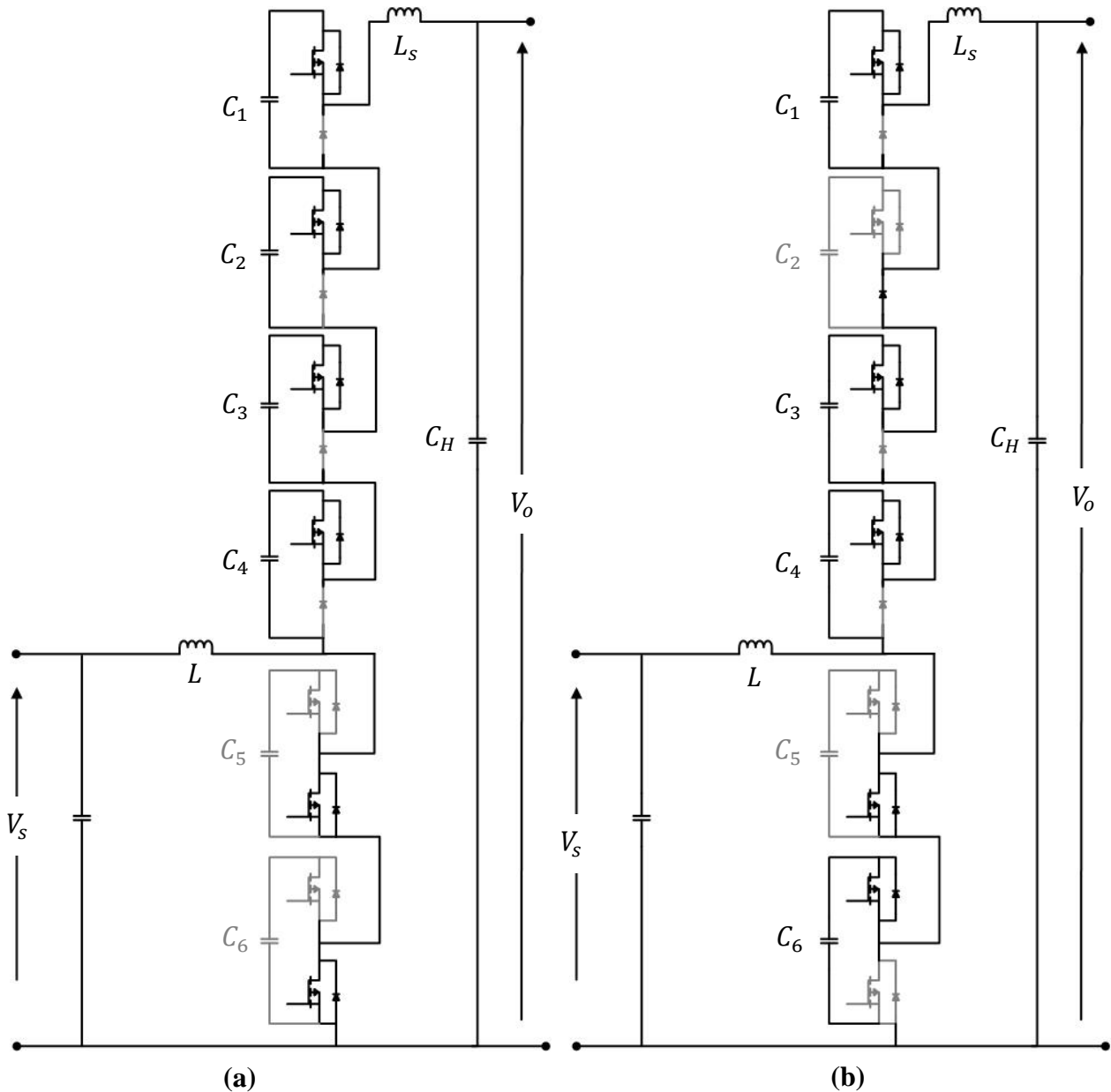
Fig. 2.3. A high step-up transformerless MMC during (a) mode 1. (b) mode 2 [20]

10

$$v_o = N \, v_c \, , \tag{2.2}$$

where v_c is a capacitor voltage.

2.3.2   Modes 2, 4, 6, and 8

These modes can occur when one of the lower submodule's capacitors is connected to the capacitors of the upper submodules as shown Fig. 2.3 (b). In other words, three of the upper capacitors are connected in series with one of the lower capacitors. The output voltages of the modes 2, 4, 6, and 8, respectively, can be written as:

$$v_{o2} = v_{c1} + v_{c3} + v_{c4} + v_{c6}, \tag{2.3}$$

$$v_{o4} = v_{c1} + v_{c2} + v_{c4} + v_{c5} \, , \tag{2.4}$$

$$v_{o6} = v_{c1} + v_{c2} + v_{c3} + v_{c6} \, , \tag{2.5}$$

$$v_{o8} = v_{c2} + v_{c3} + v_{c4} + v_{c5} \, , \tag{2.6}$$

where v_{o2}, v_{o2}, v_{o2}, and v_{o2} are the output voltages during modes 2, 4, 6, and 8, respectively.

Based on (2.3), when v_{c2} is absent v_{c6} compensates for it. The same phenomena are happening for $v_{c5,}$ and v_{c6} which compensate for the absent capacitor's voltage as indicated in (2.4) through (2.6). Consequently, by comparing (2.3) with (2.5), equation (2.7) results in:

$$v_{c2} = v_{c4} = v_{c6}. \tag{2.7}$$

Similarly, by comparing (2.4) with (2.6), equation (2.8) is written as:

$$v_{c1} = v_{c3} = v_{c5} \, . \tag{2.8}$$

11

From the above analysis, it can be concluded that the upper submodule's capacitor voltages are balanced by the lower submodule's voltages. Therefore, it shows how that the closed-loop controller can be implemented in a direct manner.

2.4   Transformerless MMC Analysis

As is was previously mentioned that modes 2, 4, 6, and 8 have the same on states. In addition, modes 1, 3, 5, and 7 have the same operational configuration. Therefore, operation of the transformerless MMC can be divided into two modes. Select mode 1, that is the same as 3, 5, and 7, and mode 2, which is the same as 4, 6, and 8. To simplify the theoretical analysis, suppose the capacitor dc voltages of all submodules are the same.

When the MOSFET in submodule 1 is on, then mode 1 begins, and it ends when the MOSFET in submodule 2 is switched off. In mode 1, the input voltage is equal to the voltage of the low side inductor L. In addition, the current of that inductor is charged by the lower cells through MOSFET 5 and 6. At the same time, when the input current i_L starts charging, the current of the upper cells i_N starts rising from zero, and the lower cells current falls down to the minus. During this mode the equivalent circuit is shown in Fig. 2.4.
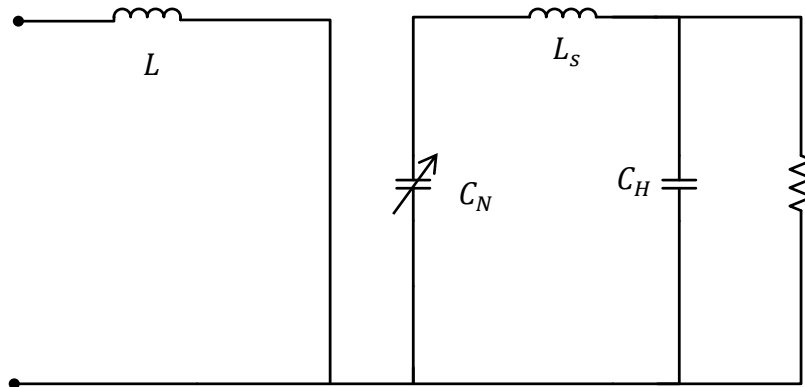
Fig. 2.4. Mode 1 equivalent circuit of the transformerless MMC.

During mode 2, the capacitor in submodules 2 and 5 are out of the series connection, and the capacitor C_6 is connected with the capacitors of the upper submodules C_1, C_3, and C_4, together with the resonant inductor L_r and the output capacitor C_H as shown in Fig. 2.5. According to [19] and [20], the resonant frequency can be written as:

$$f_r = \frac{1}{2\pi\sqrt{L_r C/N}} \tag{2.9}$$

During mode 1 input voltage is equal to the low side inductor current v_S, from that the peak to peak ripple current of inductor L is:

$$\Delta I_L = \frac{v_s}{L} t_{on} \tag{2.9}$$

where $t_{on} = dT_e$. By using KVL for mode 2, input voltage is equal to the sum of inductor current and voltage of the lower cells. Therefore, the peak to peak ripple current of inductor L is:

$$\Delta I_L = \frac{v_{Ci} - v_s}{L} t_{off} \tag{2.10}$$
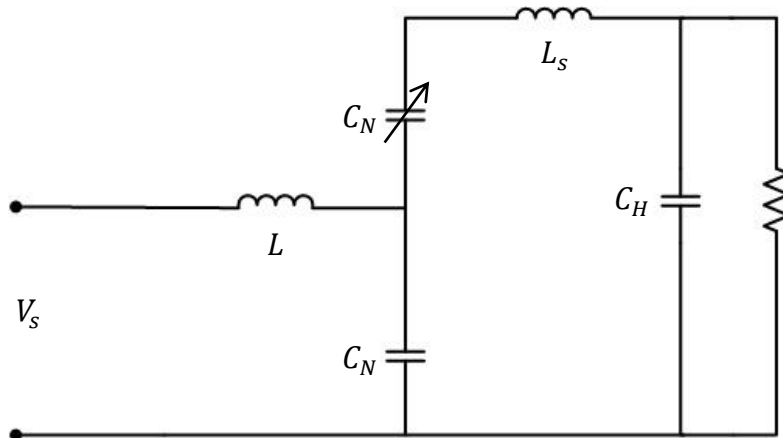
Fig. 2.5. Mode 2 equivalent circuit of the transformerless MMC

where t_{off} is the off time and equal to $(1 - d)T_e$, and i=5 or 6. By using the derivation in [20], for steady-state conditions for the volt-second balance on the inductor, the capacitor of the lower cells has a well defined peak-to-peak ripple current and voltage conversion ratio. Due to the previous analysis and with an assumption that $t_{on} = t_{off}$ and $T_e = t_{on} + t_{off}$, equations (2.9) and (2.10) can be written as

$$\frac{v_s dT_e}{L} = \frac{(v_{Ci} - v_s)(1 - d)T_e}{L} \tag{2.11}$$

and the peak-to-peak current for the low side inductor ΔI_L from charging and discharging time can be written as:

$$\Delta I_L = \frac{v_s dT_e}{L} . \tag{2.12}$$

From (2.11), the voltage of the lower cells can be written as

$$v_{Ci} = \frac{v_s}{1 - d} . \tag{2.13}$$

The output voltage is the sum of the upper and lower submodules voltages, $v_O = v_N + v_M$. Therefore, the output voltage could be written as

$$v_O = \frac{N - 1 + d}{N} \sum_{i=1}^{N} v_{Ci} + \frac{1 - d}{M} \sum_{i=N+M}^{N+M} v_{Ci} \tag{2.14}$$

By solving equations (2.2) and (2.13), the voltage conversion ratio is given by

$$\frac{v_o}{v_s} = \frac{N}{1 - d} . \tag{2.15}$$

14

If the capacitor voltages are balanced for all the submodules and equal to v_C, the voltage conversion ratio can be found by substituting (2.12) into (2.13), so the voltage conversion also can be found to be the same (2.15).

The voltage conversion ratio depends on both N and d. For example, if the duty cycle is 0.58 and the number of the upper cells is equal to 4, then the conversion ratio is approximately 9.5. By adjusting the duty cycle and choosing the suitable number of upper cells, the voltage conversion ratio can be 1:10.

According to [20] the current conversion ratio can be written as:

$$I_s = \frac{N}{1-d} I_o \tag{2.16}$$

From equation (2.16), the input current should be ten times the output current.

2.5   Step-down Transformerless MMC

The transformerless MMC can also operate as a high step-down converter as shown in Fig. 2.6. In the step-down topology, v_o is defined as the output voltage in the step-up operation and is considered as the input voltages during the step-down. However, v_s is the step-down output voltage. The step-down also has eight modes as in step-up. By using the same assumption for step-up modes, modes 1 and 2 can be selected for simplified purposes.

Mode 1 starts when the MOSFETs in submodule 1 and 2 are turned off, as shown in Fig. 2.7 (a). C_1, C_2, C_3, and C_4 are in series, and creating resonant tank. During mode 1, the summation of the capacitor voltages of the upper cells gives the step-down input voltage, v_o, as

$$v_o = v_{c1} + v_{c2} + v_{c3} + v_{c4}. \tag{2.17}$$

15
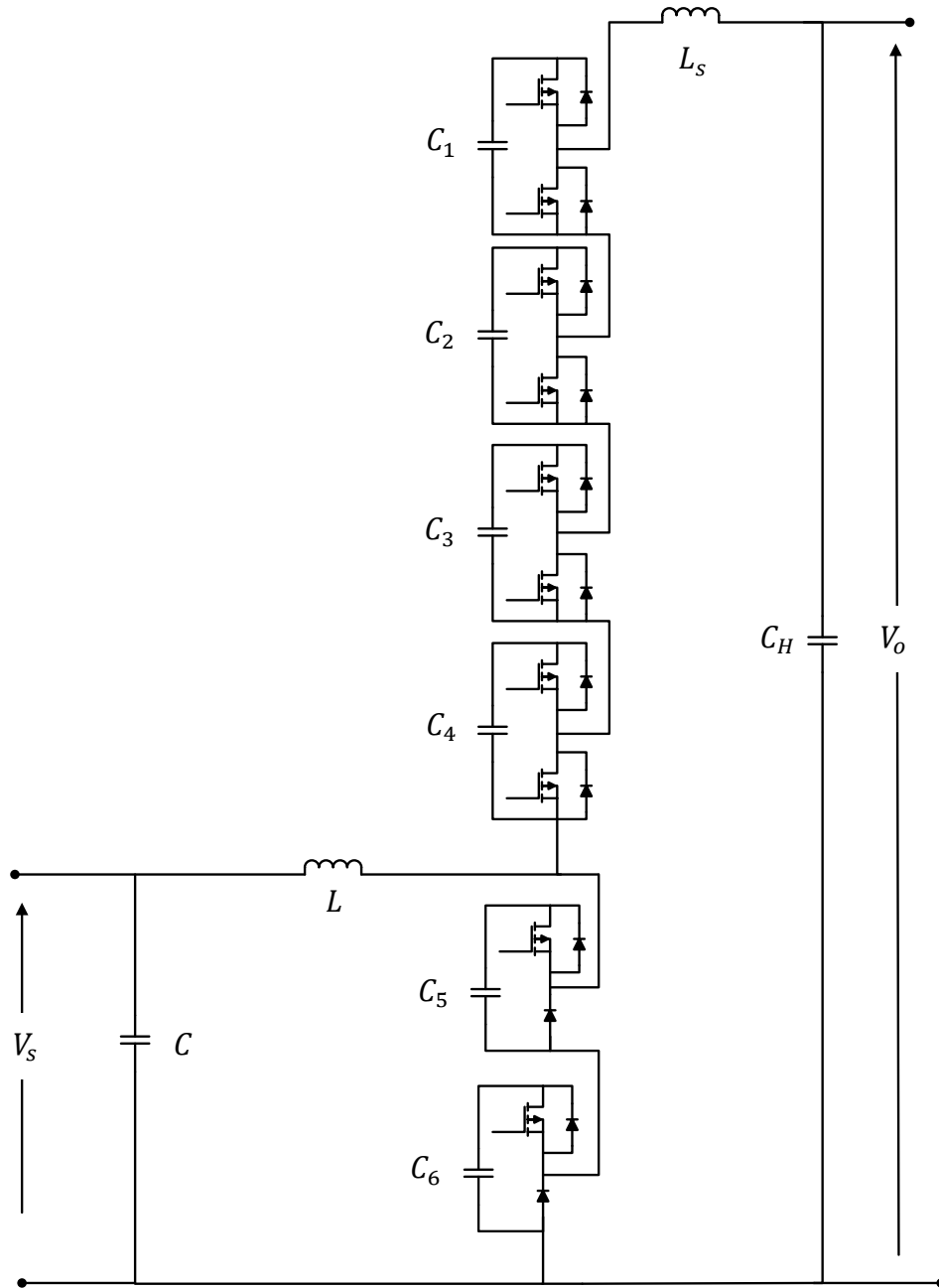
Fig. 2.6. A high step-down transformerless MMC [20].
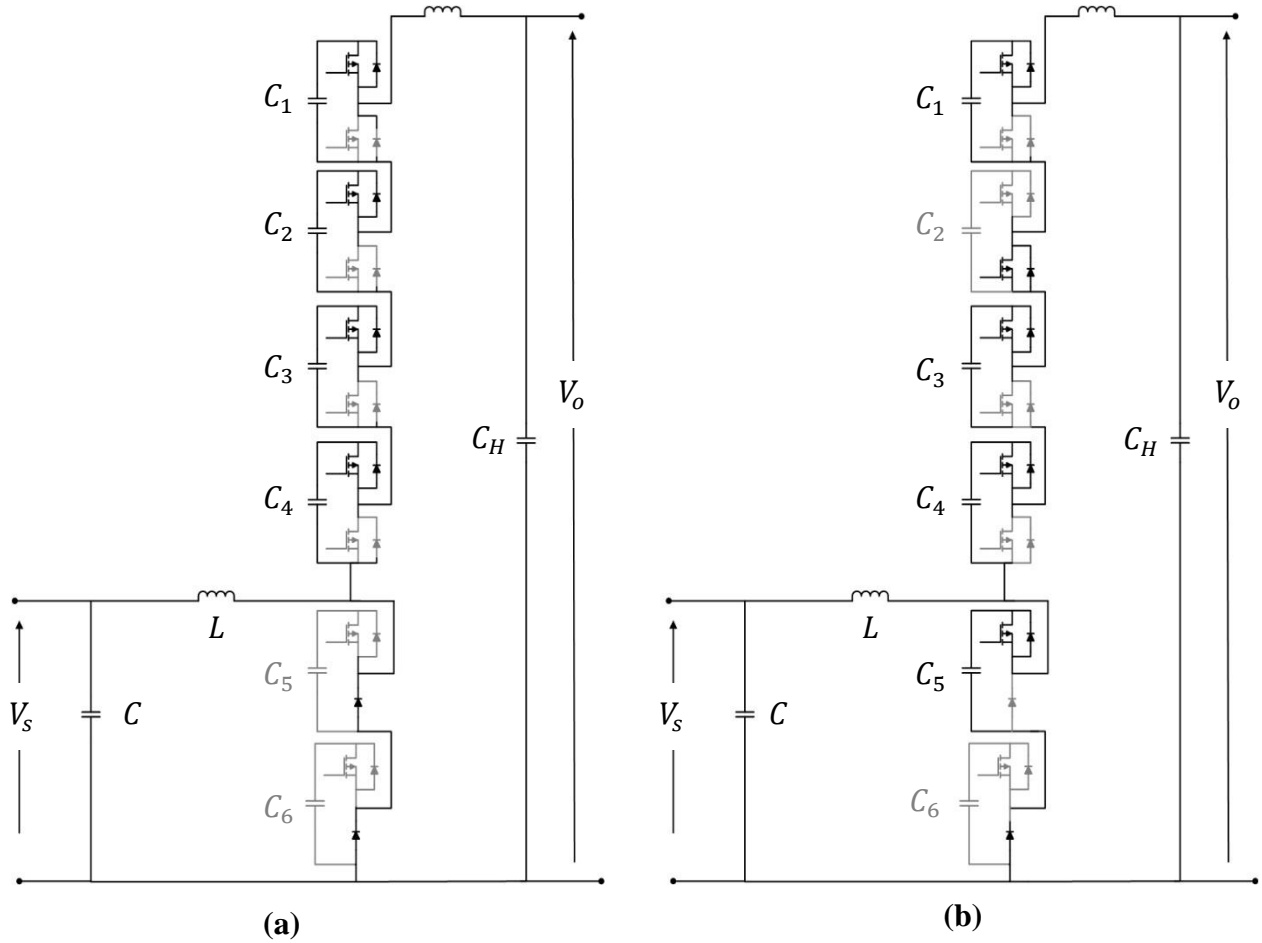
Fig. 2.7. A high step-down transformerless MMC during (a) mode 1. (b) mode 2 [20].

During mode 2, MOSFETs in the submodules 2 and 6 are turned on so that their capacitors are absent during this mode as shown in Fig. 2.7 (b). Therefore, C_1, C_3, C_4, and C_6 are in series with the resonant inductors. In addition, the sum of the voltages of these capacitors can be written as:

$$v_o = v_{c1} + v_{c3} + v_{c4} + v_{c6} \tag{2.18}$$

Even though (2.18) is similar to (2.3), it should be noted that v_o is the step-down input voltage, not the output voltage. From (2.17) and (2.18) the input voltage can be simplified as

$$v_o = N\, v_{ci}. \tag{2.19}$$

Using the same analysis for step-up, the voltage of the lower capacitors is the same as

(2.13). Therefore, solving (2.13) and (2.19) gives the conversion ratio for the step-down mode,

and it could be written as

$$\frac{v_o}{v_s} = \frac{N}{1 - d}. \tag{2.20}$$

2.6 Bidirectional Transformerless MMC

Since equations (2.15) and (2.20) are the same, this type of transformerless MMC can

operate as a bidirectional dc-dc converter. The bidirectional can be accomplished by making the

direction of the current to be opposed without changing the switching PWM. The bidirectional

topology is shown in Fig. 2.8.

Fig. 2.8. A high step-up/down (bidirectional) transformerless MMC [20].

CHAPTER THREE

SIMULATION RESULTS OF THE TRANSFROERLESS MMC

3.1   Introduction

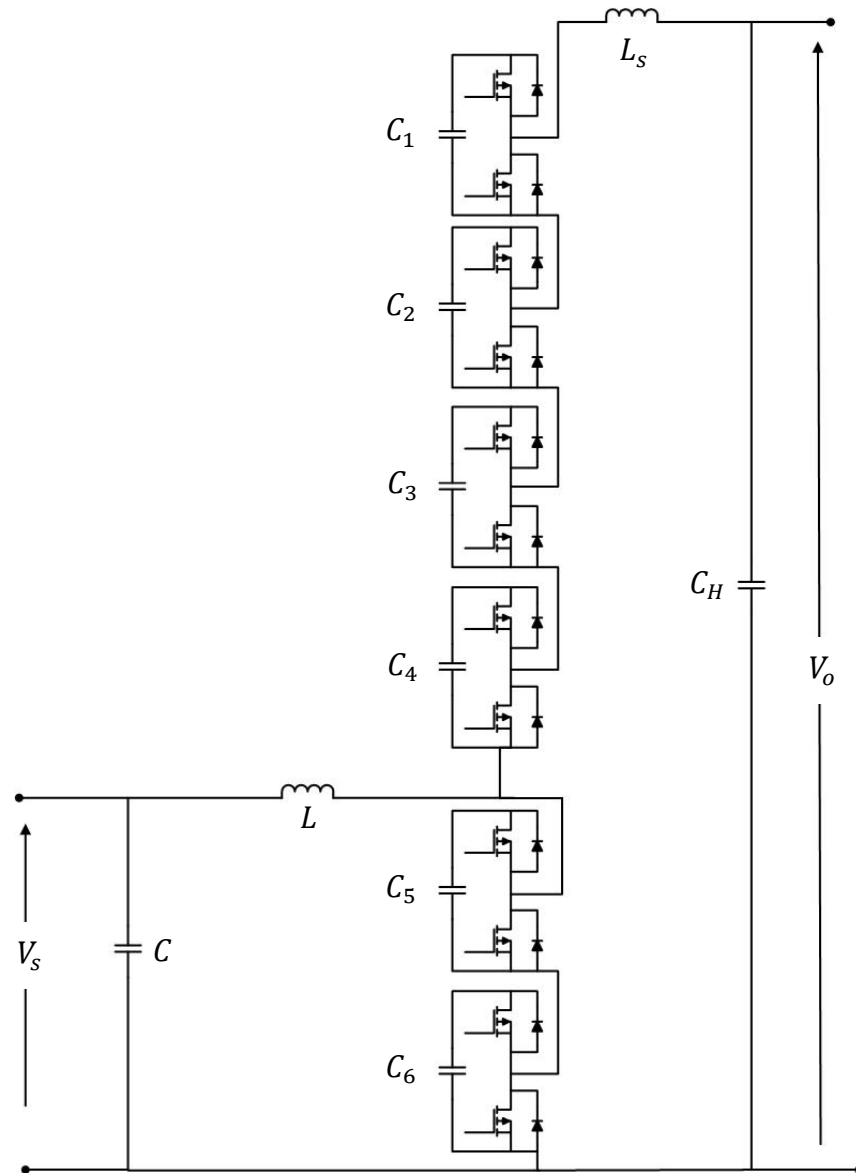Chapter Two derived all the possible operating modes for the MMC. Simulation results using MATLAB-Simulink are now presented for step-up, step-down and bidirectional operating conditions.

3.2   Simulation Results for Step-Up and Step-Down MMC

The open-loop system was implemented in MATLAB/Simulink™. The detail of how the simulation was configured is given in Appendix A.1. The conversion ratio was 1:10 for step-up and 10:1 for step-down. The input voltage is selected to be 30 V and the output voltage is 300 V. The parameters for step-up topology are listed in Table 3.1.

The output voltage of the step-up voltage is shown in Fig. 3.1. When mode 1 starts, i_L is charged by the load, and voltage, i_M starts to rise. When mode 1 ends and mode 2 begins, i_L reduces because the voltage on cell 6 is higher than input voltage. Before the end of mode 2, i_N falls to zero, and i_M and i_L are the same. That result proves that the $i_L = i_N + i_M$. The simulation results for, i_L , i_N and i_M are shown Fig. 3.2.

The step-down topology has the same parameters as Table 3.1 [20]. The output voltage of the step-down is 30 V when the input is 300 as shown in Fig. 3.3. The current waveforms of the step-down are shown in Fig. 3.4.

Also a detailed LTspice analysis model has been developed and is detailed in Appendix A.2. Simulation results indicate the benefits that are expected from the theoretical intent. The conversion ratio was 1:10 for step-up and step-down.

C2M0080120D-SiC Power MOSFET models from CREE were used for LTspice simulation purposes. The CREE MOSFET can operate up to 1200 V, but in this application, the MOSFET operates from 30 V to around 100 V. This reduced voltage operation is used for a low-power prototype to first demonstrate proof of concept. When the low-power circuit operation is verified then a high-power version can be implemented with confidence.

Table 3.1. Parameters of the simulation example for step-up [20].

Symbol	Quantity	Value
v_L	Low dc output voltage	30 V
v_H	High dc input voltage	300 V
C_N	Upper submodule capacitor	50 μF
C_M	Lower submodule capacitor	50 μF
C_H	High voltage side capacitor	120 μF
L_S	Output side inductor	821μH
L	Low voltage side inductor	120 μH
R_H	High voltage side resistor	600 Ω
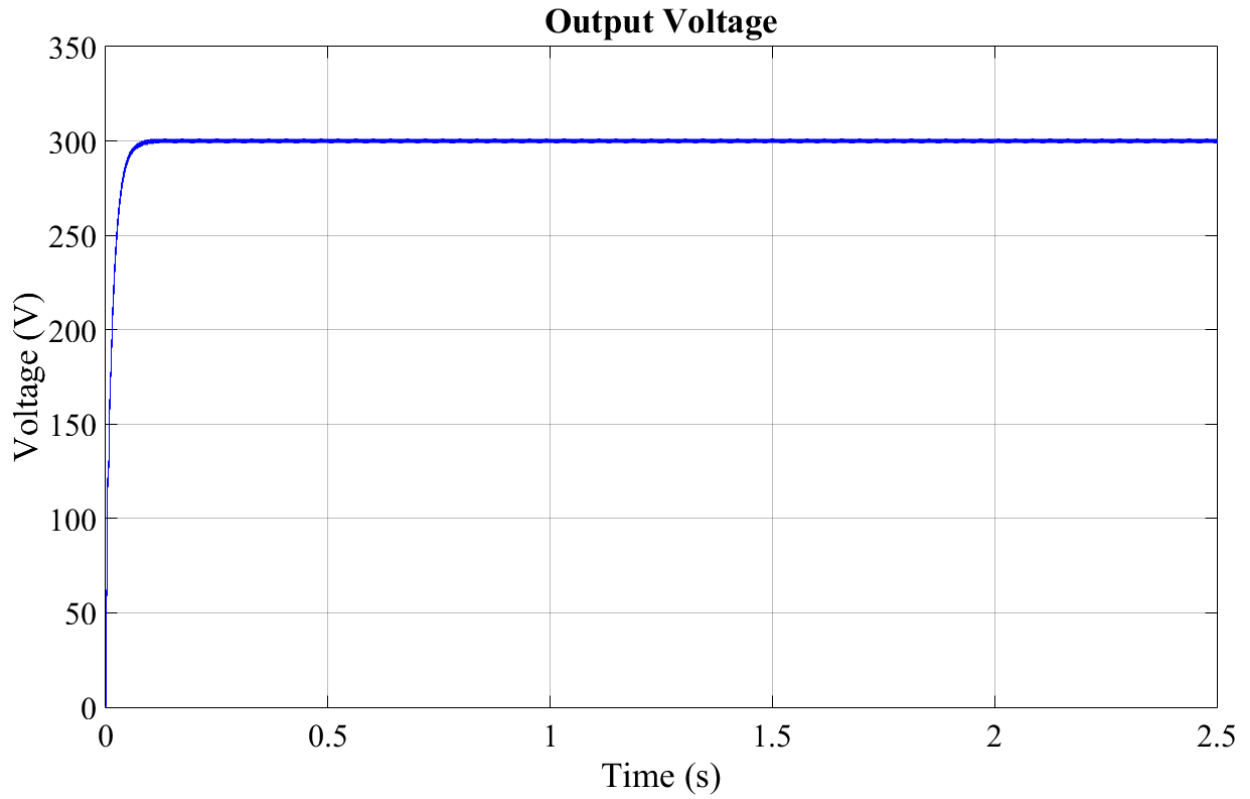
Fig. 3.1. MATLAB Simulation output voltage waveform of the closed loop system.
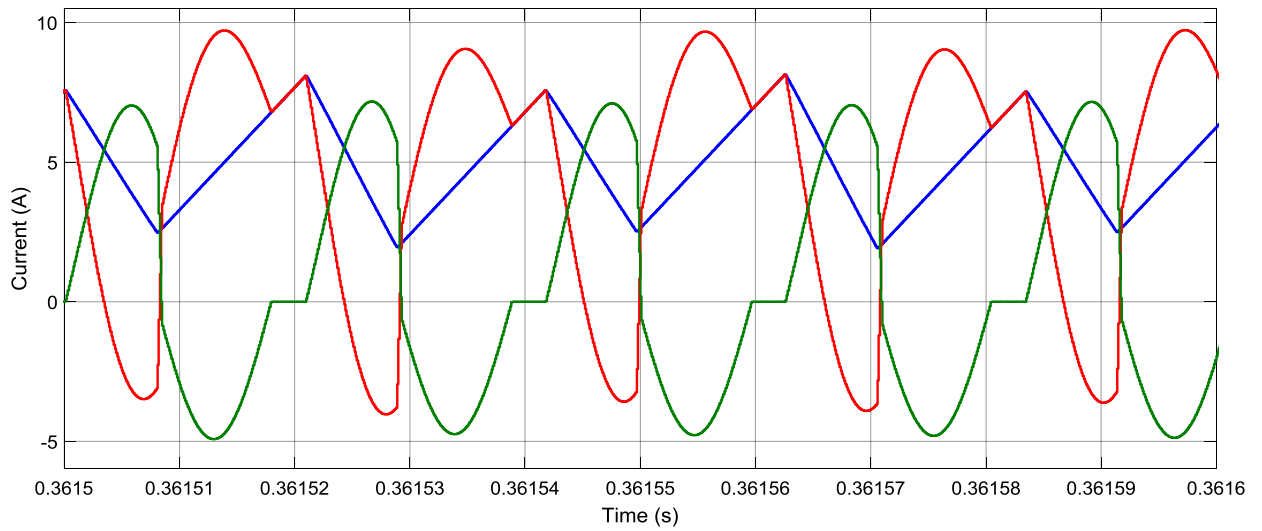
Fig. 3.2. Input current (blue), upper submodules current (green), lower submodules current (red).

Fig. 3.3. Output step-down voltage.
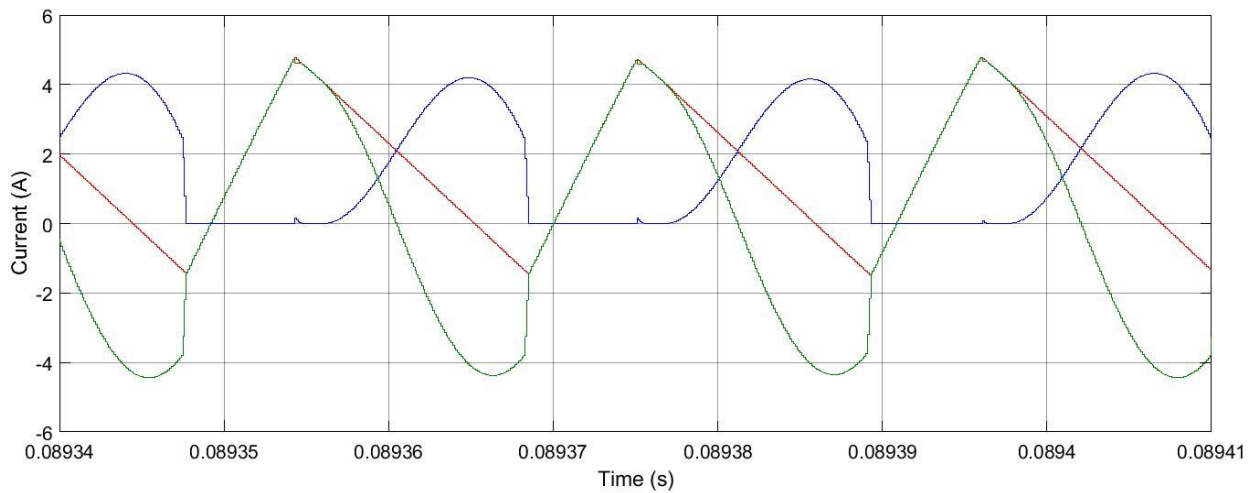
Fig. 3.4. Input current (blue), upper submodules current (green), lower submodules current (red), for step-down.

The simulation is based on CREE SiC power MOSFET PSPICE library by using LTspice software shows the same MATLAB/Simulink™ results. Also, for purposes of designing the gate drivers, CREE C2M MOSFET SPICE models predict the gate current and gate to source voltage for each MOSFET. The output voltage is 300V when the input voltage is set to be 30V as

expected. Figs. 3.5 and 3.6 show the output voltage and current waveforms simulated by LTspice, respectively.
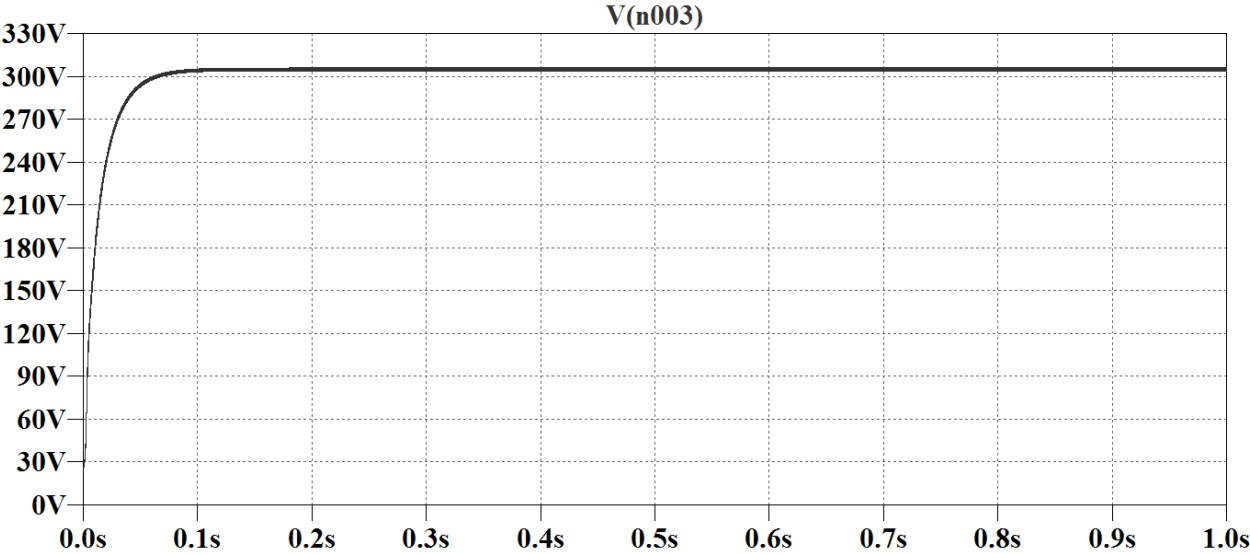
Fig. 3.5. LTspice Simulation output voltage waveform.
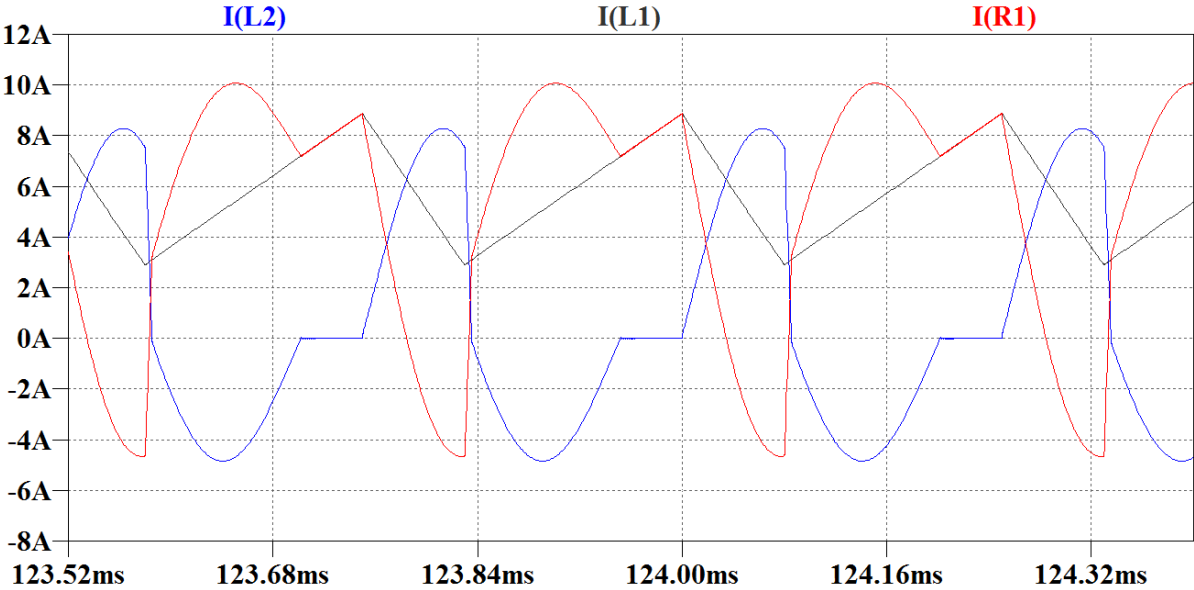
Fig. 3.6. Input current (blue), upper submodules current (green), lower submodules current (red).

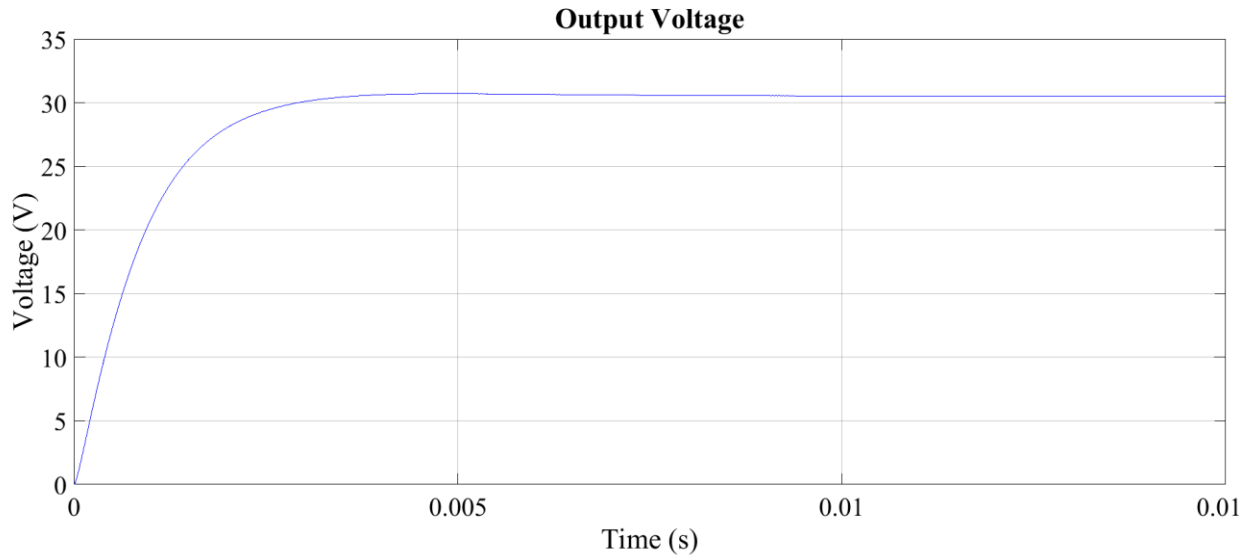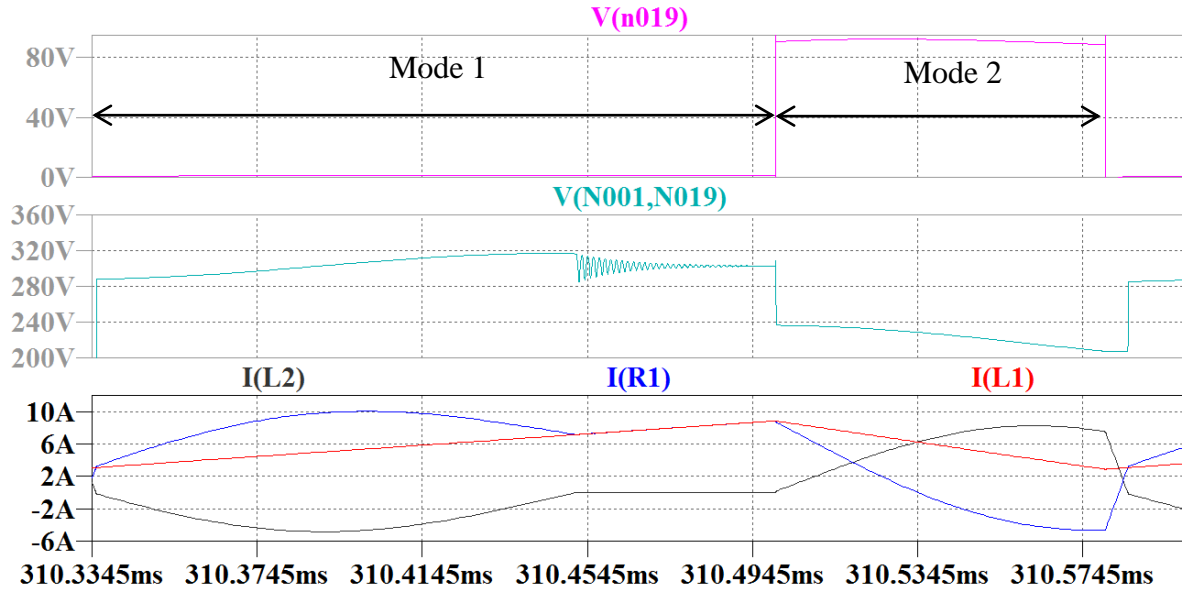**Fig. 3.7. Lower submodules (top) and upper submodules (middle) voltages and current waveforms (bottom) during modes 1 and 2.**

Fig. 3.7 shows modes 1 and 2. During mode 1, the lower submodules' voltage is zero due to the fact that there is no capacitor connected to the output inductor. However, the upper submodule's voltage is around 300 V. This mode is represented in Fig. 2.4 in Chapter Two. During mode 2, the output voltage is the sum of the upper and lower voltages.

3.3.   Bidirectional Transformerless MMC Simulation

This section presents the design of a high conversion ratio bidirectional MMC. The proposed converter steps up the input voltage with a 1:10 conversion ratio. Also, during the step-down operation mode, the MMC can buck the voltage with a 10:1, as given in Appendix A.3.

The system has been simulated using MATLAB/Simulink™. The input voltage in this simulation is 30 V for the step-up, and the output voltage is 300 V. Fig. 3.8 shows when the MMC transits from step-down to step-up at t=2.5 s. From (2.15), the voltage conversion ratio

25

depends on both the number of the upper cells, *N,* and the duty cycle, *d.* To have a 1:10 conversion ratio, the number of the upper cells sets to be 4, and the duty cycle 0.6. The operation frequency is 80 kHz. The complete circuit parameters are listed in Table 3.2.

Table 3.2. Parameters of the bidirectional simulation.

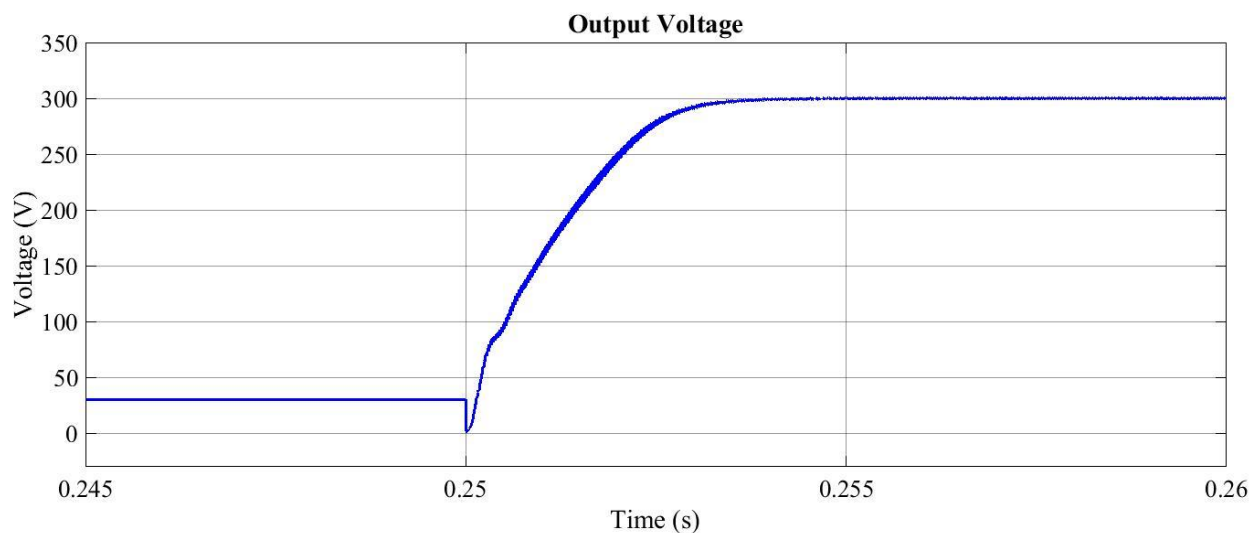| Symbol	Quantity	Value
v_L	Low dc output voltage	30 V
v_H	High dc input voltage	300 V
C_N	Upper submodule capacitor	4.17 μF
C_M	Lower submodule capacitor	4.5 μF
C_H	High voltage side capacitor	36 μF
L_S	Output side inductor	10 μH
L	Low voltage side inductor	68 μH
R_H	High voltage side resistor	600 Ω

Fig. 3.8. Transition from step-down (from 300 to30V) to step-up (from 30 to 300 V).

26

CHAPTER FOUR

GATE DRIVER DESIGN

4.1   Introduction

This chapter presents the experimental results for designing a gate driver for a SiC MOSFET. The MOSFET was switched using a simple gate driver circuit and chip. Using a reasonable gate driver circuit is important to ensure the proper operation of the MOSFET. Opto-isolation is used to separate the digital control signals from the analog circuit. Opto-isolation is simple to implement and has very fast response to switching signals. Opto-isolators also help to remove electrical interference from source and load variations in the circuit. Once isolation is achieved, the gate driver is designed, then the output of the MOSFET is observed. This chapter confirms the feasibility of switching at least one FET for potential application of the entire circuit with acceptable transient switching behavior.

4.2   Gate driver design

To drive a SiC MOSFET, the voltage should be higher than the threshold voltage. For the silicon-carbide Cree MOSFET, the turn-on/off voltages are 20/-5 V. Using the Texas Instruments UCC27531 gate driver chip, the gate driver circuit schematic is shown in Fig. 4.1 [21]. Isolation is required between the input signal and the gate driver, to avoid excessive current draw and voltage loading issues. The SI8261BCC-C-IS opto-coupler was used to perform such isolation and can provide up to 4 A of current.
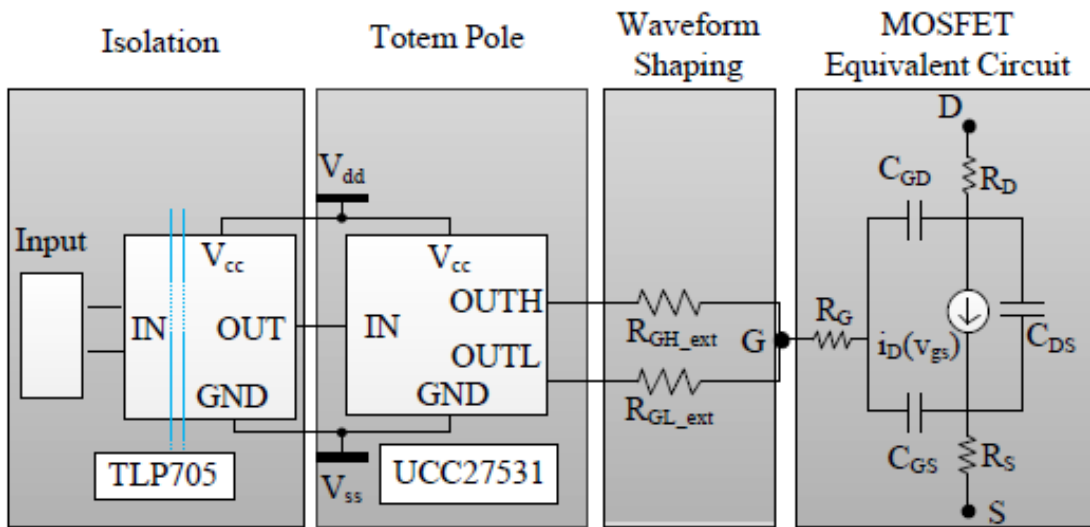
Fig. 4.1. Gate driver setup [21]

The gate driver circuit provided by [21] was designed in a schematic using OrCAD Capture, then the PCB layout was completed using Allegro PCB Editor. The board was then milled out on the Accurate CNC 427 milling machine, populated with the appropriate circuit components then tested in the lab for correct operation. The circuit drove a CREE MOSFET and its gate-source, drain-source voltage and drain current waveforms were acquired on an oscilloscope as shown in Fig. 4.2.

The switching times and responses seen in Fig. 4.2 and Fig. 4.3 are typical due to parasitic inductances and capacitances from traces in the printed circuit board. The inevitable parasitic behavior can be mitigated by keeping the gate driver as close as possible to the MOSFET and keeping all traces as short as possible. However, high fidelity signal integrity simulation is not so critical for this application. The switching responses are acceptable.
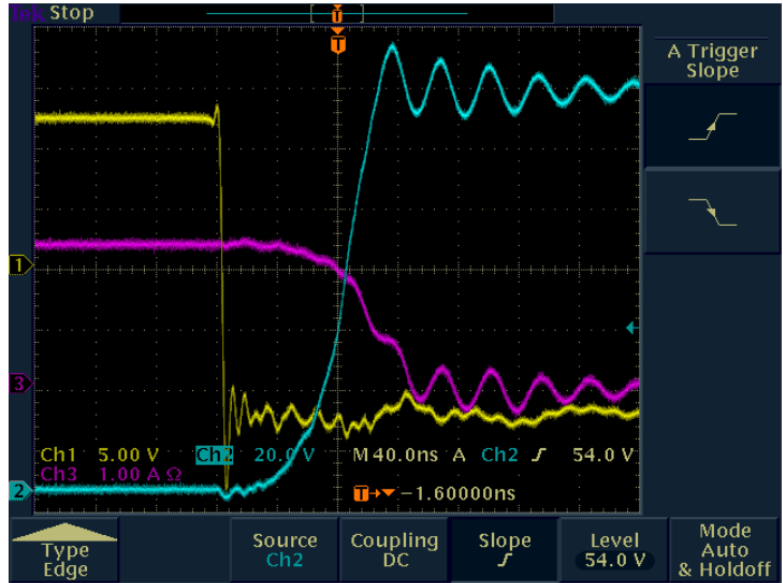
Fig. 4.2. During turn off: drain-source voltage (blue), drain current (red), gate-source voltage (yellow).
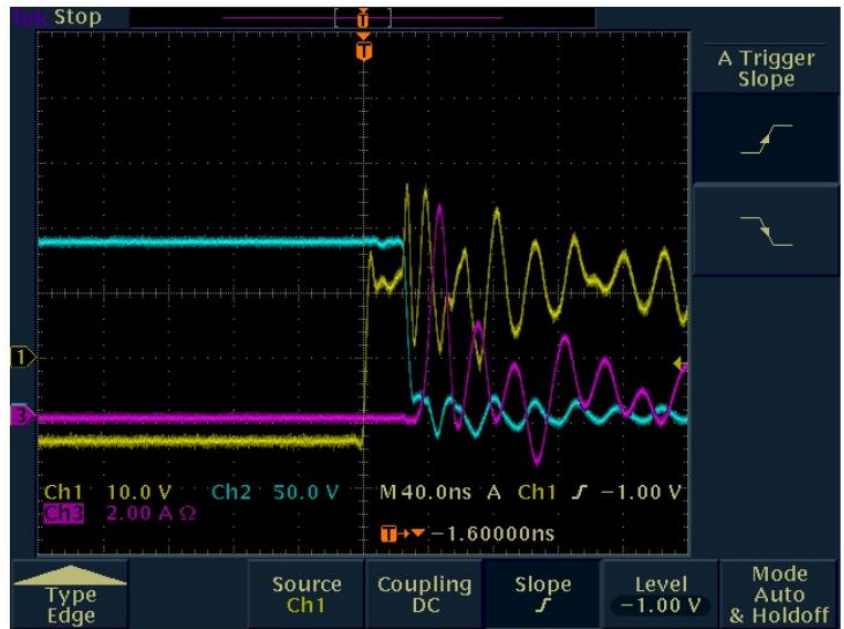
Fig. 4.3. During turn on: drain-source voltage (blue), drain current (red), gate-source voltage (yellow).

This acceptable transient behavior helps confirm the feasibility of making multiple modules for application. The layout was designed using Allegro PCB Editor and is illustrated in Fig. 4.4. As mentioned earlier, it was important to keep traces a short as feasible while still allowing room to solder the components on the board. The printed circuit board for the gate driver was milled out using the Accurate 427 milling machine from Accurate CNC Inc as shown in Fig. 4.5.
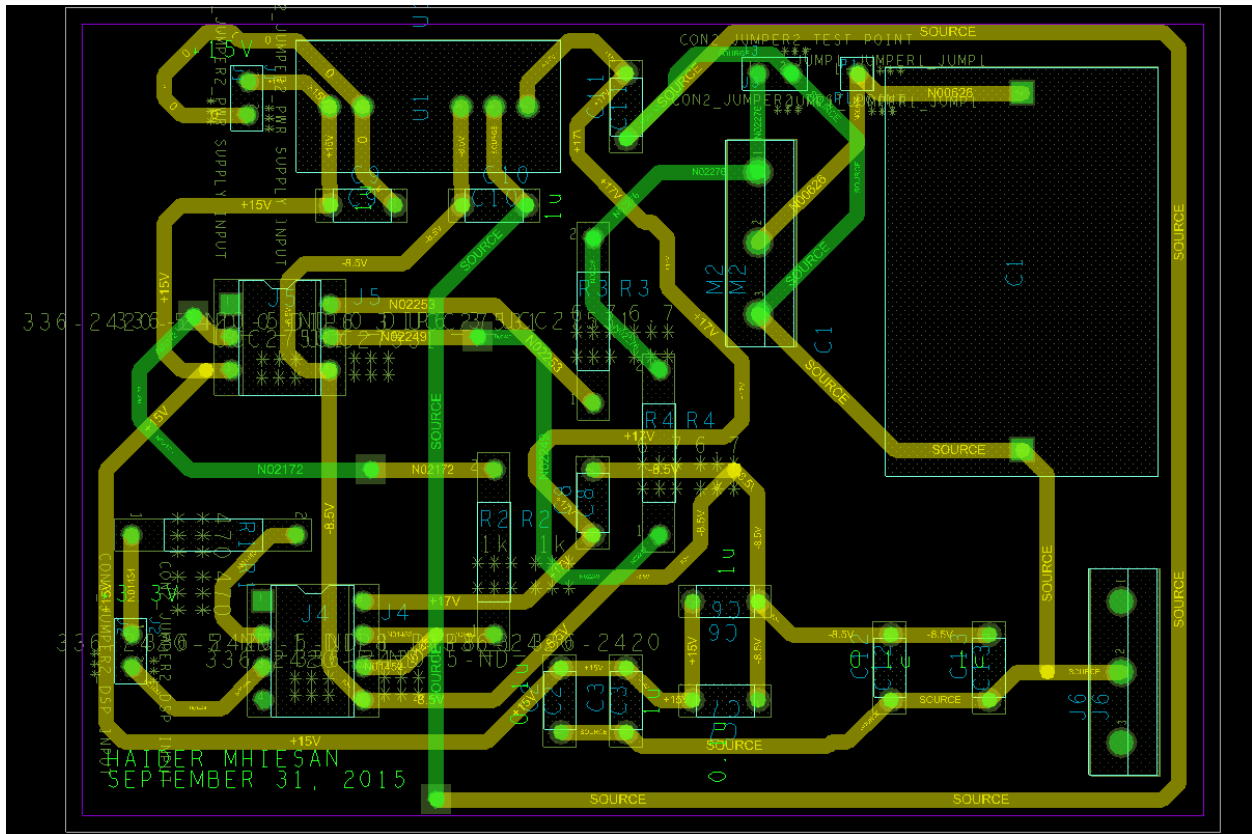
Fig. 4.4. PC board layout of gate driver circuit.
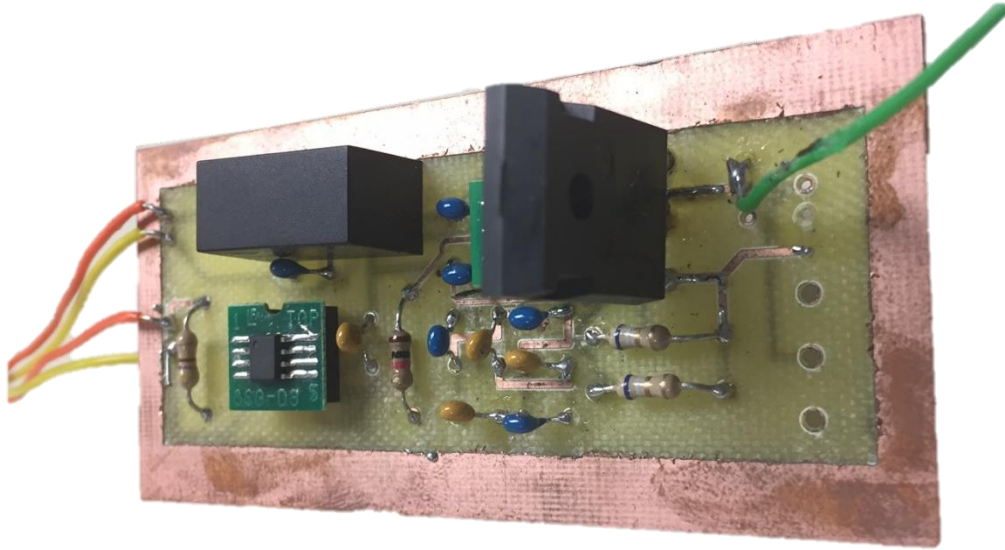
Fig. 4.5. Gate driver for a silicon-carbide MOSFET.

CHAPTER FIVE

TRANSFORMERLESS MMC FOR PHOTOVOLTAIC SYSTEMS

5.1 Introduction

The inclusion of dc power system in electric power grid is expanding rapidly because of the development of power electronics. Grid-connected photovoltaic energy conversion systems are one of the fastest growing electrical energy sources. Historically, the first PV plants were built in the 1980s as thyristor-based central inverters. In the mid-1990s, IGBT and MOSFET were used for all the types of photovoltaics. Fig. 5.1 shows the global growth in using PV system [21].

Recent converter topologies have overcome many challenges in low-scale and medium-scale PV systems. In case of having low-scale or medium-scale PV systems, challenges have been overcome since distinct converter topologies were established recently. The use of conventional methods, such as a central inventor, to link a large-scale PV plant with a dc power transmission system, however, encounters some obstacles. First, one or two step-up transformers are necessary to boost the produced voltage to the required high voltage level, and this happens due to the voltage restrictions on the dc-side of the conventional two level inverter.
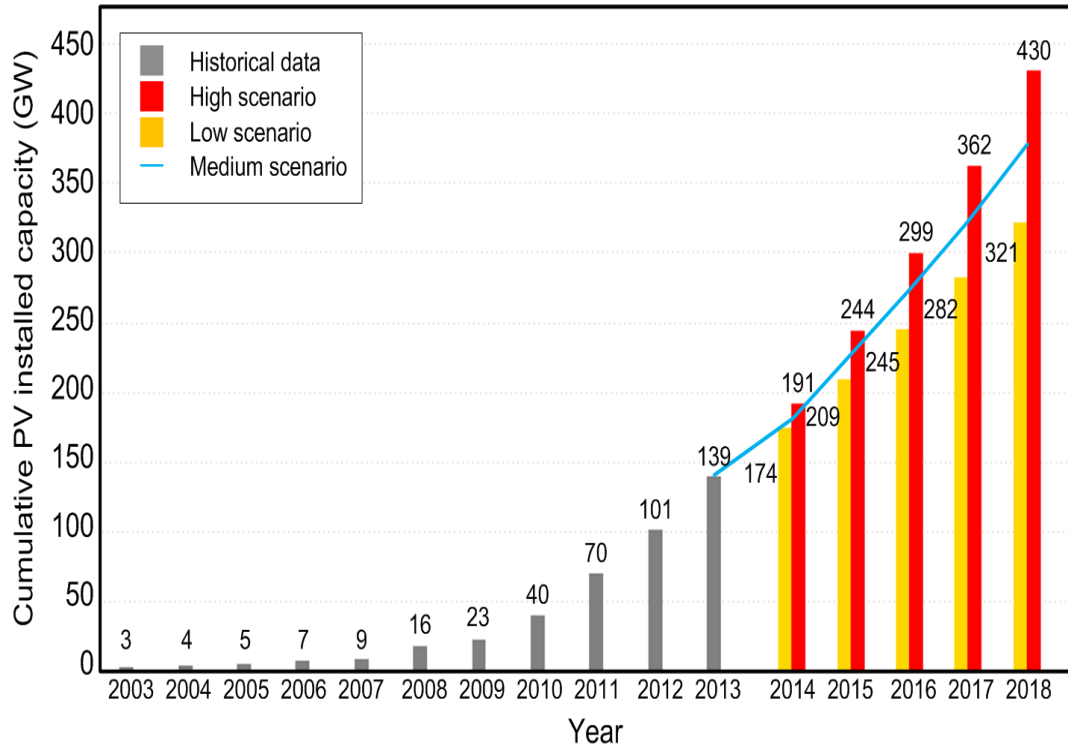
Fig. 5.1. World cumulative PV installed capacity during 2003 - 2013 and forecast during 2014 - 2018 [21].

In other words, this central converter cannot operate at high voltage levels, which makes the use of step-up transformers unavoidable. Another issue that is associated with the classical approaches of connection is the need of use two steps to connect the large-scale PV power plant to the dc power system. First, a dc-ac inverter is required before stepping the voltage up, and this can be completed by using the transformers; then, an ac-dc rectifier has to be placed in order to interface the large-scale PV system to the dc power system. Because of these restrictions, MMC is of high value since there will be no need to utilize transformers since the voltage, produced by the PV plant, is dc in natural, and MMC can achieve the high voltage level. This leads to shorten the mandatory steps of interfacing large-scale PV plants with dc power systems [22].

5.2   Isolated and Non-isolated PV systems

According to Section 690.35(G) of the National Electric Code (NEC), the system is defined as isolated when there is a transformer that is connected between the input and the output. Therefore, there is no direct connection between both the input and the output. However, if the transformer is absent, the system is referred to as a non-isolated system. The isolated system is used with grounded designs while ungrounded design includes non-isolated system [23]. Converters with transformers can connect to either another line-frequency or high-frequency transformer. Unfortunately, line-frequency transformers have many concerns such as high cost, large size and increased weight, and high-frequency transformers increase the complexity of the system [24]. The benefits of using non-isolated are: high efficiency, low cost and ground fault sensitivity [23]. The efficiency of the non-isolated converter increases since the absence of the transformer lowers the system losses. These losses typically occur as heat in the transformer core. Non-isolated systems do not have transformers and so do not have such losses, so the system becomes less costly. Therefore, new non-isolated power electronics topologies are attractive for the commercial PV arrays [25]. Fig. 5.2 shows a PV array with and without isolation.
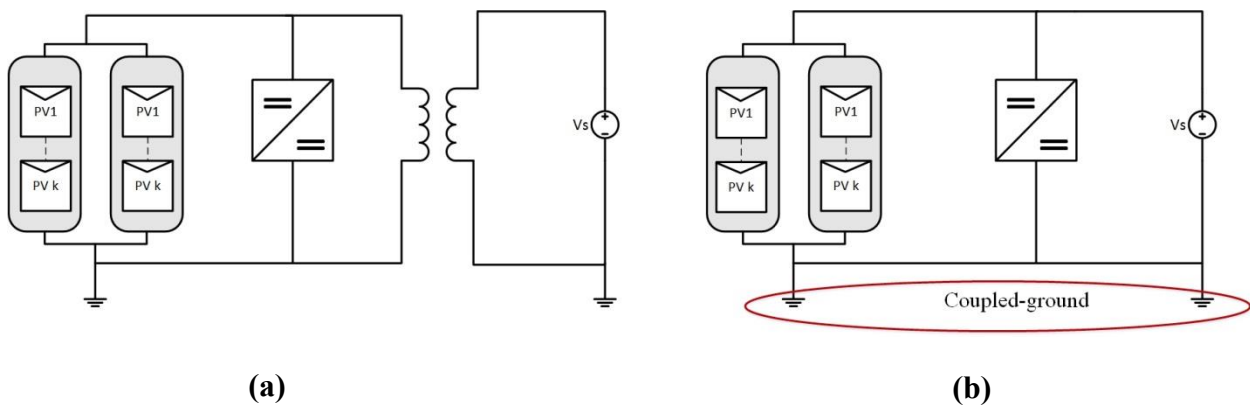

(a)   (b)

Fig. 5.2. Simple PV array construction (a) isolated (b) non-isolated systems.

In Fig. 5.2(b) there is a direct connection between the grid and the PV panels through their grounds. To prevent the problem of the coupled ground, either the ground of the PV panels or the source should be removed. NEC Section 690.35 allows to eliminate the PV panel ground.

However, there is a leakage current and safety criteria should be considered. Since there is a direct connection between the PV panels and the grid, leakage currents can be caused by potential voltage difference between the photovoltaic cells and the grid. These voltages fluctuations cause charging and discharging PV parasitic capacitances to occur. The PV parasitic capacitor is a capacitor that forms between the photovoltaic surface and the ground. The parasitic capacitance is very high within PV systems since the PV cells act as capacitors [24]-[26]. Fig. 5.3 shows the parasitic capacitance in an ungrounded transformerless MMC.
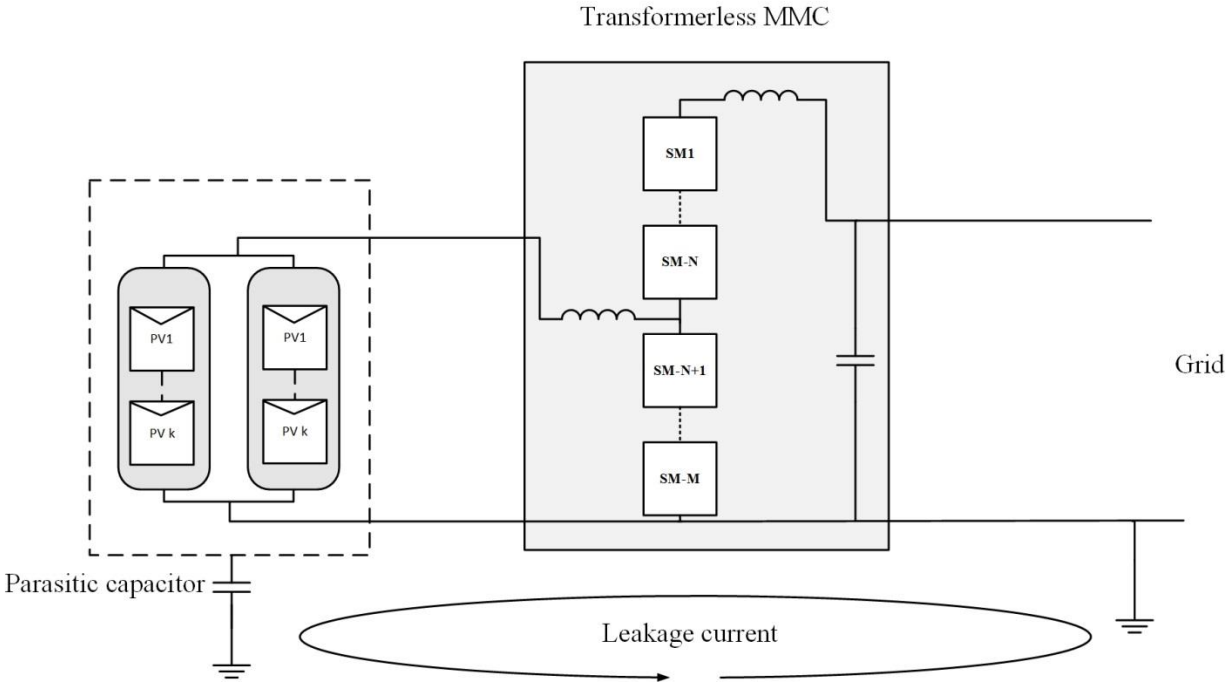

Fig. 5.3. Ungrounded transformerless MMC with PV.

The European specification VDE-0126-1-1 allows the PV to disconnect from the grid in case the leakage current is higher than 300 mA within 0.30 s. [23]-[24]. Also, UL 1741 allows using more ground fault protection detector (GFPD) fuses. These fuses are located in the positive and negative sides of the input and output voltage. According to UL 1741, the maximum trip time for sudden fault is 0.040 s at 30 mA. Also, residual current should be monitored for the PV panels. PV outgoing and returning currents should be equal to zero. This protection can define the ground fault before the fault can damage the circuit.

Using the above definitions, the circuit topology for high step-up dc-dc conversion ratio using the transformerless MMC approach is shown in Fig. 5.4. The input voltage for this converter is a set of series and or parallel photovoltaic (PV) strings. The system includes GFPD fuses and relay for protection purposes. GFPD fuses located in the input and the output to protect the circuit from faults in case it happens in the input or output side.

As shown in Fig. 5.4, there are three different types of the protection circuits. GFPD fuses can be limited whether to open the line or not depending on the current amount. Relays are breakers that received their commands from the controller in case there is a fault. Input/output voltages and currents could be monitored for protection purposes. In case there is a fault, then the corresponding voltage and current amplitudes will change. The controller detects this situation and sends a command for opening the relays.

In this thesis, the fault protection system does not include the GFPD since they are commercially available. However, the controller is designed to monitor the output currents as described in the next section.
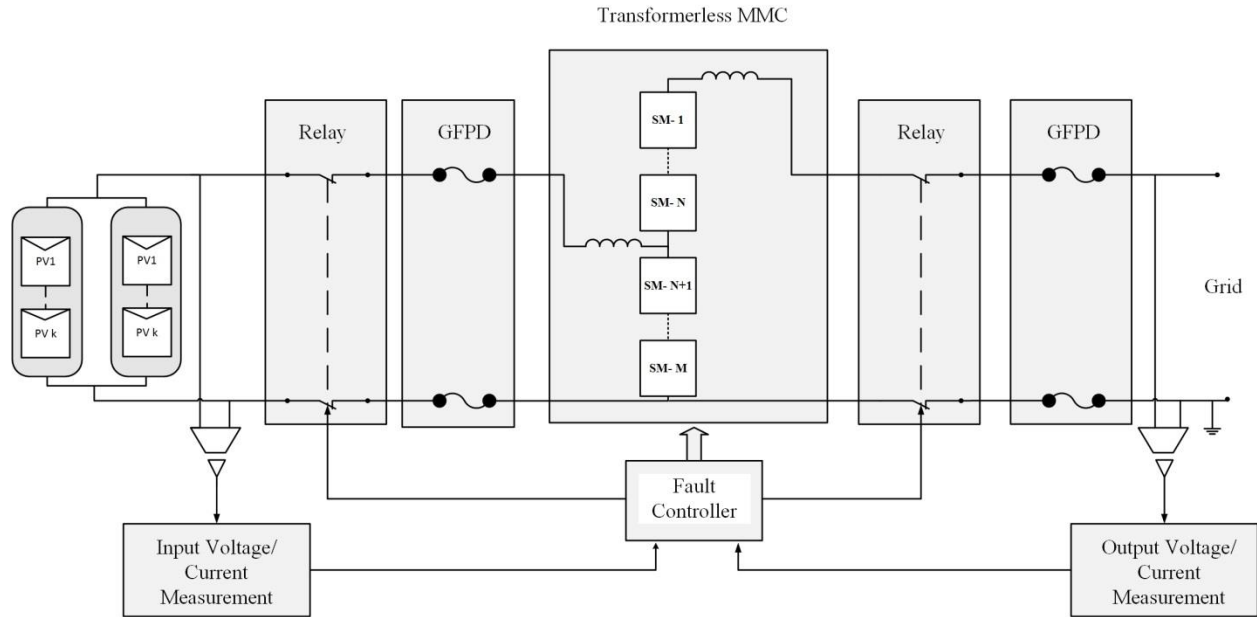
Fig. 5.4. PV system with protection.

5.3   Fault Controller for Bidirectional MMC

There is a direct connection between the input and the output. Therefore, an earth fault created on the output of the MMC will be seen by the controller. When the controller detects the fault, it sends signals to turn off the switches. In addition, the controller sends commands for the relays to be opened. Of special note is its operation when the ground fault has cleared – the converter quickly reaches maximum operating voltage. This operation is achieved by the setup in Fig. 5.5 that shows the step-up converter fault at the output side.

The controller monitors the output current with a reference value. After comparing the set reference with the average current, the result goes to MOSFETs pulse disable. The controller turns off the MOSFETs when output current (average) is greater than the reference, otherwise, the MOSFETs remain operational. When the controller detects the faults, and turns off all the

MOSFETS, it sends a command for the relays to separate both the input and the output voltage. In this case, there is no direct connection between the PV panels and the grid as shown in Fig. 5.6. When the fault is cleared and the relays are closed by the user, the controller starts to operate again as shown in Fig. 5.7.
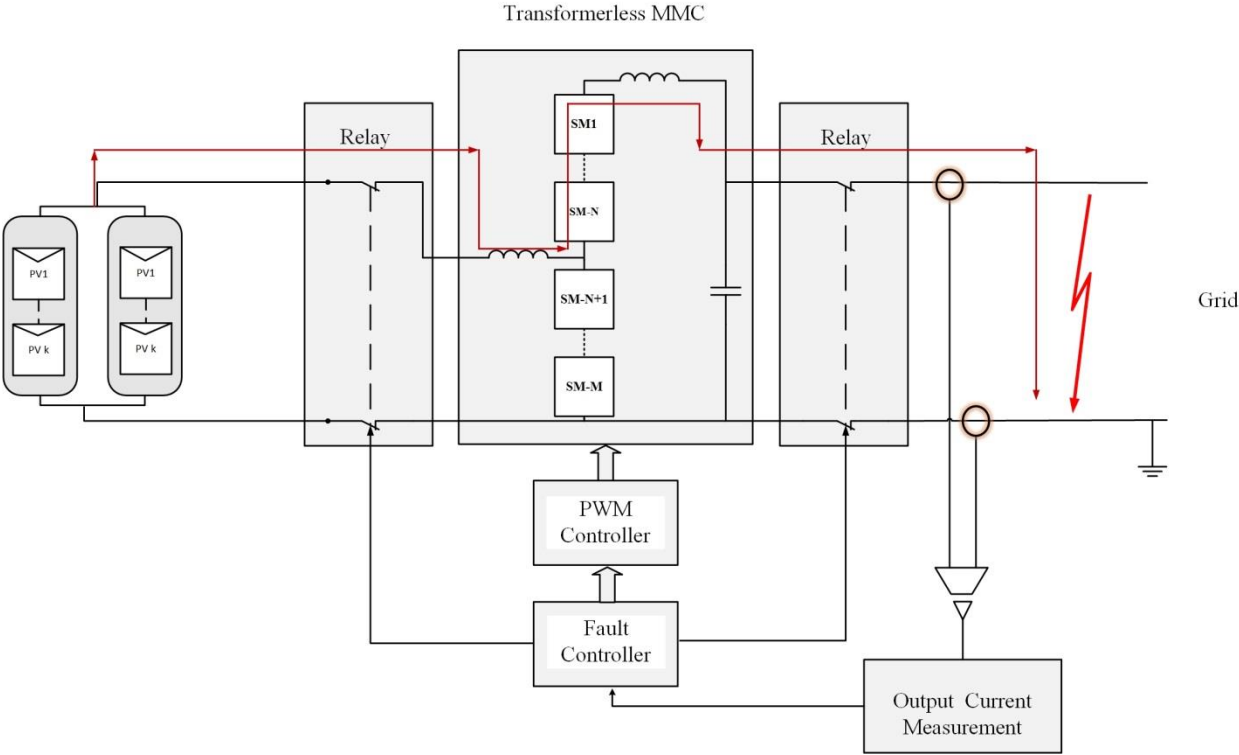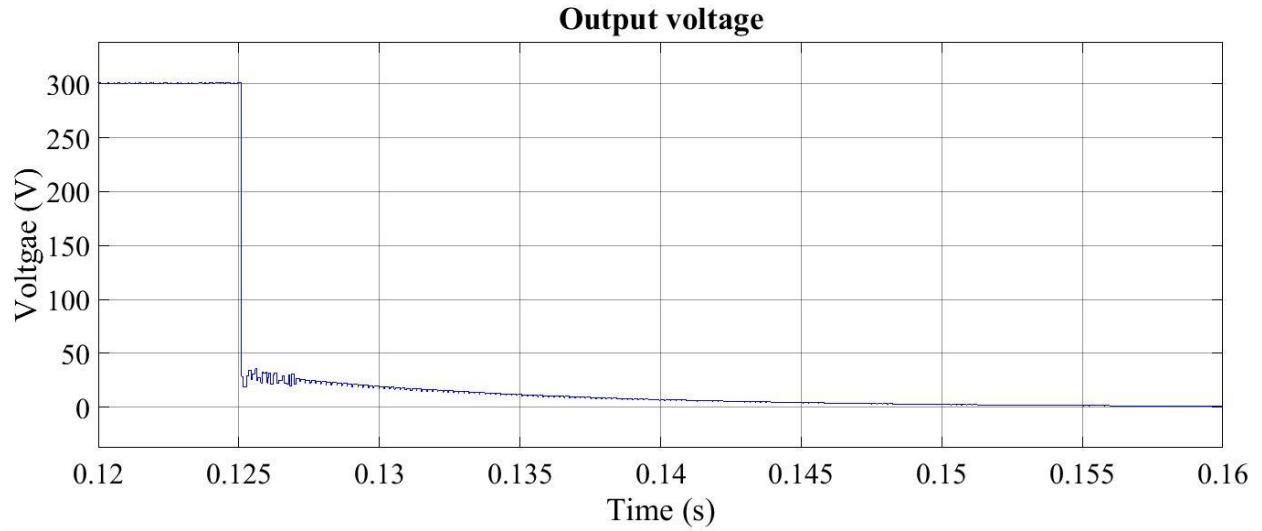

Fig. 5.5. Fault protection system.
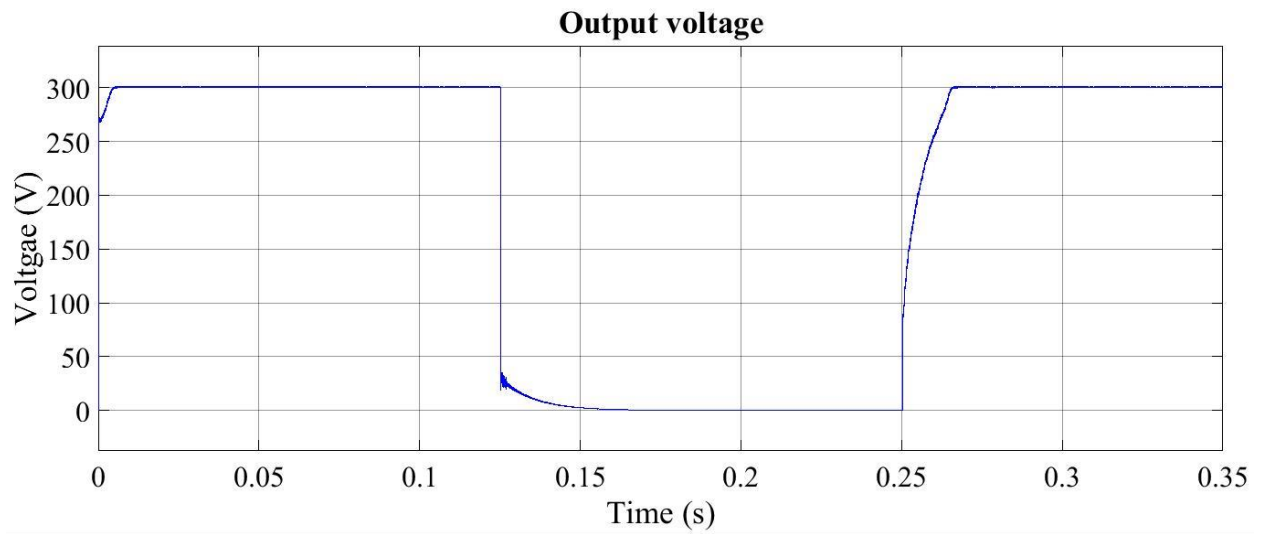
Fig. 5.6. Output voltage fault at t=1.25.

Fig. 5.7. Output voltage fault at t=1.25, at t=0.25 the fault is cleared.

5.4   Closed-Loop Controller

The MATLAB/Simulink™ is used for this closed-loop controller. The closed loop test is done by changing the input voltage and observing the output voltage. It has been done by changing the input voltage due to the fact that the PVs arrary could not supply a constant voltage. Therfore, this topology with this closed loop simulation provides a type of voltage regulator. A refrence voltage of both the input and output are used, and the closedloop provides a change in the gate driver accordingly. If any change in the input voltage is occours, the system will compensate for that change by increasing or decreasing the PWM signals. That will ensure the high voltage side of the converter , which is dc power grid, has a constant voltage for changing in the input voltage. Also, the grid voltage should be measured to ensure that it is constant. The closed-loop controller is detailed in Appendix B.

Fig. 5.8 shows the output voltage for the closed-loop control mode with input voltage that ranges from 29 V to 39 V. The input volatge in this case is a non-linear function of the PV panel variable voltage range depending on the solar insolation leavel. It shows a constant output voltage of 300 V. The controller is shown compensating for input voltage fluctations such that the output voltage is constant and equal to 30 kV as shown in Fig. 5.9.
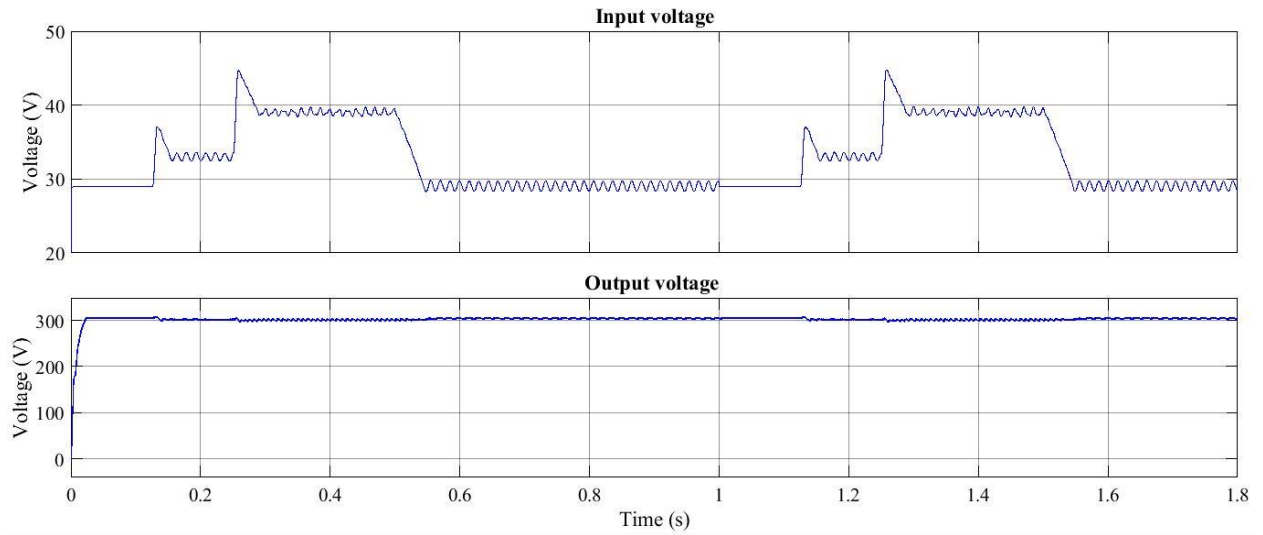
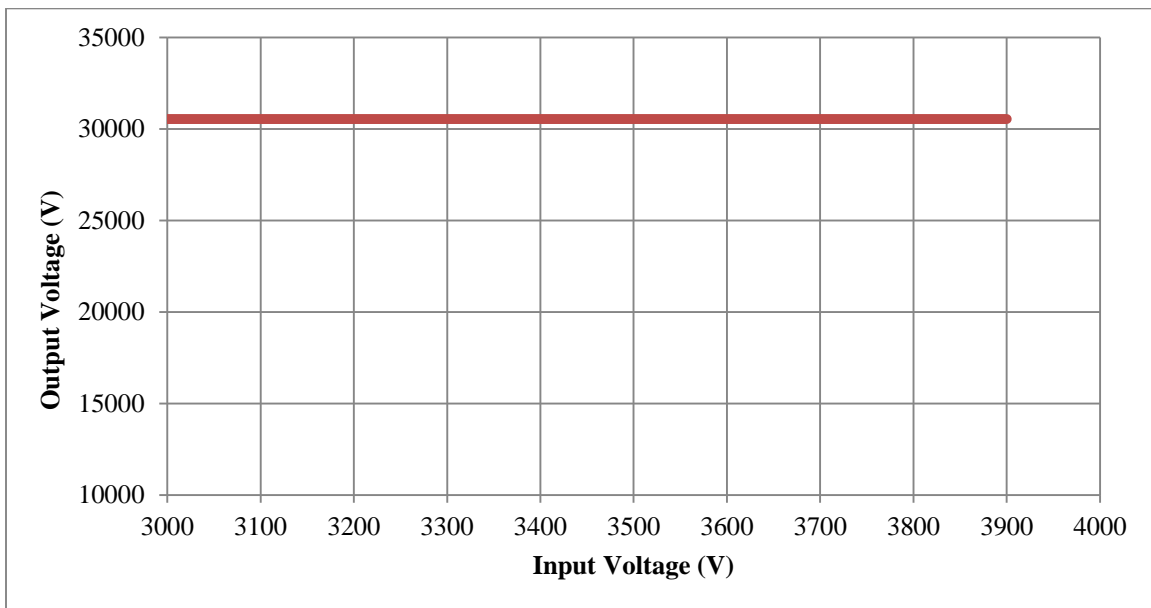**Fig. 5.8. (top) Non-linear input voltage (bottom) MMC output voltage.**

Fig. 5.9. Simulation result with changing in the input voltage.

CHAPTER SIX

A TRANSFORMERLESS MMC FOR UPS SYSTEMS

6.1   Introduction

The importance of this chapter is explaining the basic idea of the fundamental operation and controller system for an Uninterruptible Power System (UPS). The last section of this chapter incudes the application of transformerless MMC for UPS systems. This chapter analyses, discusses, and implements frequency and the voltage drooping method since it is the most practical method to control UPS systems. This chapter is similar to the techniques and assumptions as in [28]-[35].

The system for a UPS that connects to a microgrid is shown in Fig. 6.1 [28]. The bidirectional converter is used to convert the dc battery voltage into ac voltage when the UPS supplies the voltage to the grid. However, the ac voltage from the grid can be converted by the converter to the battery, and the converter operates as a buck converter.   Due to the fact that the inverter has low impedance, the harmonic currents flow into the inverter.   LCL is used to increase the output impedance. As a result, it improves THD. To measure the active and reactive power flow, there are many techniques. One of them is the frequency and voltage drooping method. To measure the mean power from the instantaneous power, a low pass filter (LPF) is utilized. Both the average and instantaneous power are the same in a balanced system. Therefore, there is no need for LPF. However, LPF is very important in unbalanced systems due to the ripple content. In this case, the ripple content of the power is eliminated by the LPF. In other words, the filter blocks the ripple of the power to affect the frequency and voltage [28]-[30].

Two different modes for the energy storage system that connects with microgrids can be defined. Battery charging modes occur when the batteries are charged by the grid. The battery receives its power from the grid. The inverter in this case inverts the ac voltage from the grid to dc voltage on the dc-link capacitor. The voltage steps down from the dc-dc converter. Also, the voltage of the dc-link capacitor is regulated by the inverter controller.

The second mode is when the batteries discharge their voltages to the ac grid. The dc-dc converter steps up the battery voltage operating as a boost converter and regulates the voltage of the dc-link capacitor. The inverter during this mode is operating as dc-ac inverter.

The controllers of both the ac-dc inverter during charging mode and the boost converter during discharging mode share regulating the voltage of the dc-link capacitor. This problem can be solved by setting two different reference voltages of dc-link capacitor. $V_{dclink-1}^*$ is the reference voltage of the boost converter during discharging mode. However, the reference voltage of the inverter is $V_{dclink-2}^*$. The reference voltage of the inverter should be higher than the reference voltage of the boost converter. To understand that, the scenario in [28] is used.
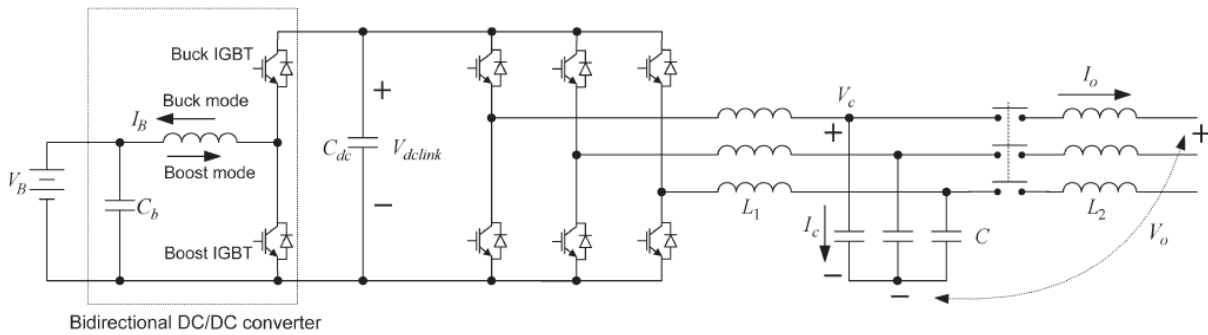

Fig. 6. 1. UPS system diagram [28].

When the system is in charging mode, the voltage of the dc-link capacitor is adjusted by the inverter. The converter runs as buck converter to charge the batteries. When a fault happens for any reason, the power flow in the inverter reverses its direction from the UPS to the grid. At that time, the voltage of the dc-link capacitor discharges into the grid. As a result of this, the voltage diminishes in the dc-link. Therefore, when the $V^*_{dclink-2}$ becomes less than $V^*_{dclink-1}$, and the converter operates as a step-up converter (boost) providing the energy to the grid.

6.2   Inner Loop Controller

From Fig 6.2 (a), the output voltage without virtual inductance is [29]:

$$V_o = G(s)V_c^* - Z(s)I_o ,\qquad(6.1)$$

where $G(s)$ is the closed loop transfer function, and $Z(s)$ is the system output impedance. $G(s)$, and $Z(s)$ can be written as [30]

$$G(s) = \frac{k_v+1}{L_1Cs^2+k_cCs+k_v+1} ,\qquad(6.2)$$

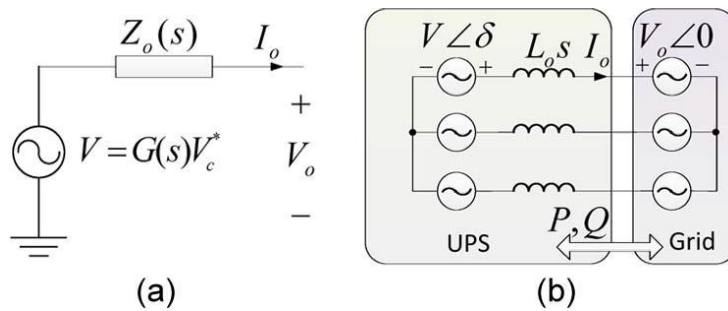$$Z(s) = \frac{L_1s}{L_1Cs^2+k_cCs+k_v+1} + L_2s.\qquad(6.3)$$

(a)   (b)

Fig. 6. 2. (a) Thevenin equivalent circuit , (b) three phase equivalent circuit [28].
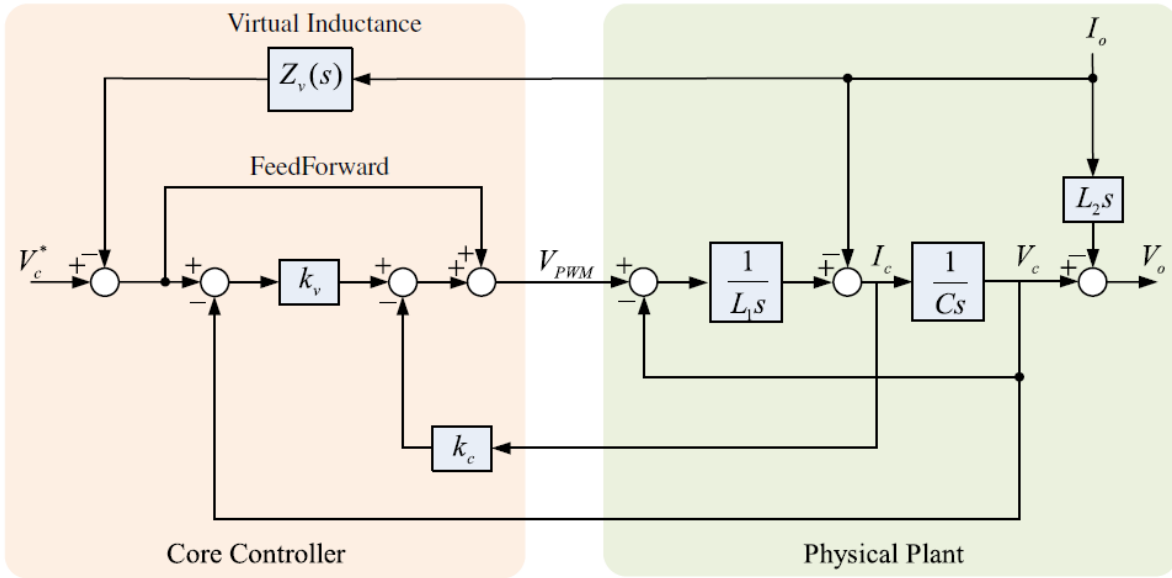
Fig. 6. 3. Block diagram of single phase inner loop [28].

where k_c, and k_v are the current and voltage gains.

6.3   Virtual Impedance

The virtual impedance method that has been used in [29]-[30] is to improve the current quality in grid connection mode. From Fig. 6.2(b), the inverter output current can be found in terms of the UPS and grid voltages and the impedance between them. The harmonics current is calculated by the grid voltage harmonics and inverter output impedance.

The virtual inductor transfer function can be written as [29],

$$Z_v(s) = sL_v,$$ (6.4)

where Z_v, and L_v are the virtual impedance and inductor. However, the above equation is in a derivation expression. Achieving that expression results in noise amplification. Therefore, a low pass filter can solve this problem, and it is written as

$$Z_v(s) = \frac{w_c s}{s + w_c} L_v \, , \tag{6.5}$$

where w_c is the filter cut off frequency. Appling (6.5) for L_v, the output voltage and inverter output impedance can be written as

$$V_o = G(s)V_c^* - Z_o(s)I_o \, , \tag{6.6}$$

$$Z_o(s) = Z(s) + G(s)Z_v(s) \, . \tag{6.7}$$

The inverter output impedance increases the rejection of the harmonics when its value is high. Bode plot for both inverter output impedance and system output impedance is shown in Fig. 6.4. It is clear from Fig. 6.4 that the inverter output impedance is greater than the output system impedance when the frequency is less than 1 kHz. This is a desired result due to the fact
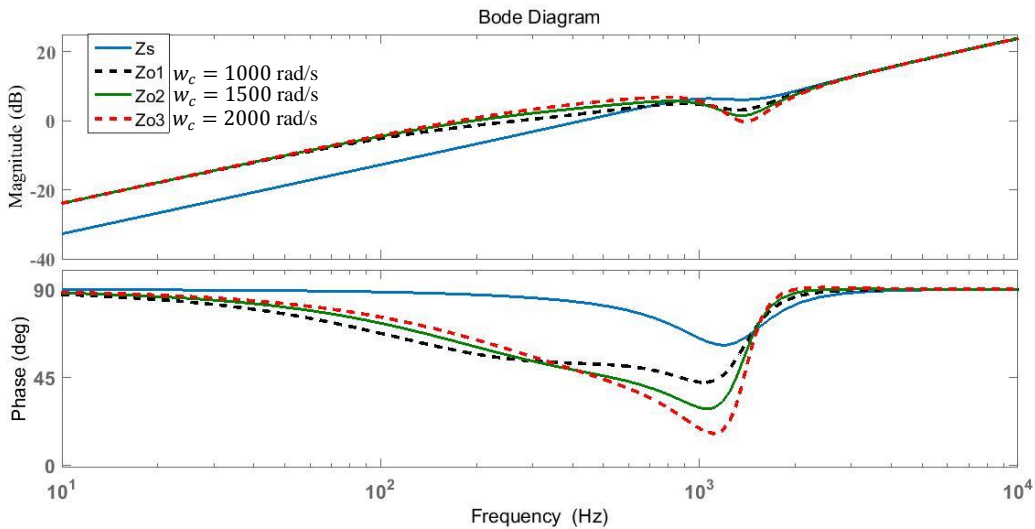

Fig. 6. 4. Bode diagram of $Z_o(s)$ and $Z(s)$.

that it can increase the harmonic rejection when $Z_o(s)$ is high. Also, it is obvious from Fig 6.4 that when the cut off frequency reduces, the inverter output impedance also reduces. That results in a reduction in the ability to reject the harmonics current.

6.4   Power Flow Equations

The drooping control can be written as [28-30]

$$\omega = w_o^* - k_w(P - P^*), \tag{6.7}$$

$$V = V_o^* - k_a(Q - Q^*), \tag{6.8}$$

where w_o^*, V_o^*, k_w, and k_a are defined in [29] as nominal frequency reference, nominal voltage reference, proportional frequency drooping coefficient, and proportional voltage drooping coefficient.

The frequency of the inverter and grid are the same in steady state. Also, the inverter output voltage is approximately equal to the grid voltage. This means from (6.7) and (6.8) that $P = P^*$ and $Q = Q^*$.

In case there is change in the load power, then the voltage and frequency of the inverter is not the same as the grid. To solve this problem, a proportional- integral (PI) controller is used to cancel the power differences between the grid and the inverter. The charging mode drooping controller equations (6.7) and (6.8) can be written as (6.9) and (6.10) as functions of integral frequency and voltage drooping coefficients, k_{w_I}, and k_{a_I} [28-30]:

$$\omega = w_o^* - (k_w + \frac{k_{w\_I}}{s})(P - P^*), \tag{6.9}$$

$$V = V_o^* - (k_w + \frac{k_{a_I}}{s})(Q - Q^*). \tag{6.10}$$

47

6.5　Small Signal Analysis

From Fig. 6.2 (b) it shows the ideal voltage source in series with L_o. Due to the fact that the impedances of the inverter and grid are different, where L_o is greater than the grid impedance, the grid impedance can be canceled. The active and reactive powers between the dc-ac inverter and V_o are [30]

$$P = \frac{3VV_o \sin \delta}{w_o L_o}, \tag{6.11}$$

$$Q = \frac{3\,(VV_o \cos \delta - V_o^2)}{w_o L_o}. \tag{6.12}$$

As was mentioned previously, the transient frequency and voltage are not the same between the inverter and the grid. The active and reactive powers have small changes, $\tilde{P}$, $\tilde{Q}$, and can be written as [29]-[30]

$$\tilde{P} = 3\frac{V_o}{w_o L_o}\,(\sin \delta_{eq}.\tilde{V} + V_{eq}\cos \delta_{eq}.\tilde{\delta}) , \tag{6.13}$$

$$\tilde{Q} = 3\frac{V_o}{w_o L_o}\,(\cos \delta_{eq}.\tilde{V} - V_{eq}\sin \delta_{eq}.\tilde{\delta}), \tag{6.14}$$

where δ_{eq} and V_{eq} as they are defined in [29] are the points where the small signal is achieved. Equations (6.9) and (6.10) can be written in terms of small signal analysis:

$$\tilde{w} = \tilde{w}_o - (k_w + \frac{k_{w\_I}}{s})(\tilde{P}^* - \tilde{P}_{avg}) \tag{6.15}$$

$$\tilde{V} = \tilde{V}_o - (k_w + \frac{k_{w\_I}}{s})(\tilde{Q}^* - \tilde{Q}_{avg}) \tag{6.16}$$

48

$\tilde{P}_{avg}$ and $\tilde{Q}_{avg}$ are defined in [30] as the change of measured average active and reactive power. To measure the active and reactive power, a low pass filter is used. $F(s)$ is the transfer function of the active and reactive power measurement and can be written as [29-31]:

$$F(s) = \frac{w_f}{s+w_f} \qquad (6.17)$$

Also, the average active and reactive power can be found by integrating the current and voltage. $F(s)$ can be represented as sliding filter as

$$F(s) = \frac{1}{Ts}(1 - e^{-Ts}). \qquad (6.18)$$

The complete block diagram of the equations (6.13) - (6.16) is shown in Fig. 6.5. The small signal block diagram model in Fig. 6.5 is simulated using MATLAB. The simulation is represented in Appendix C.1. Both equations (6.17) and (6.18) are implemented to measure the active and reactive power. The simulation results show the benefits using equation (6.18). It is clear from Fig. 6.6 and 6.7 that the sliding filter provides very fast response.
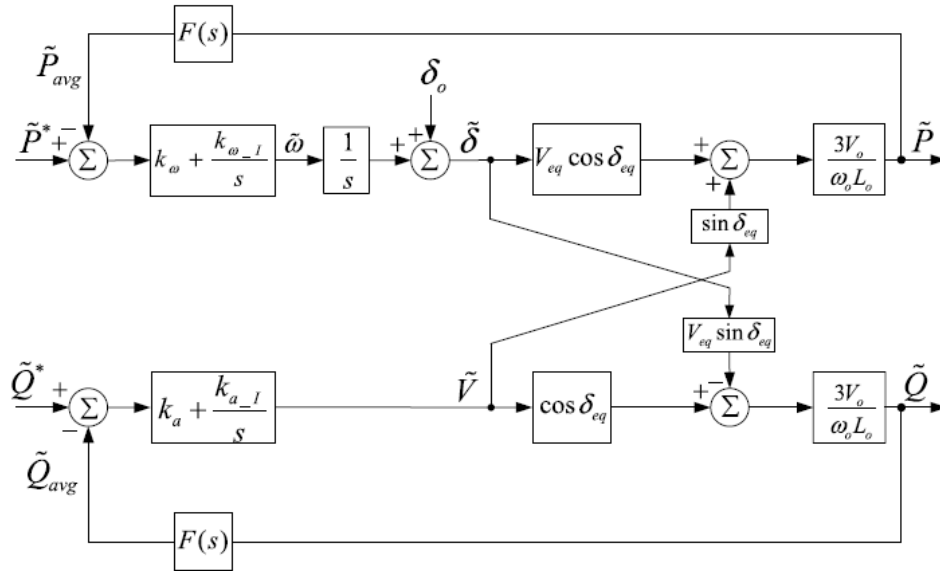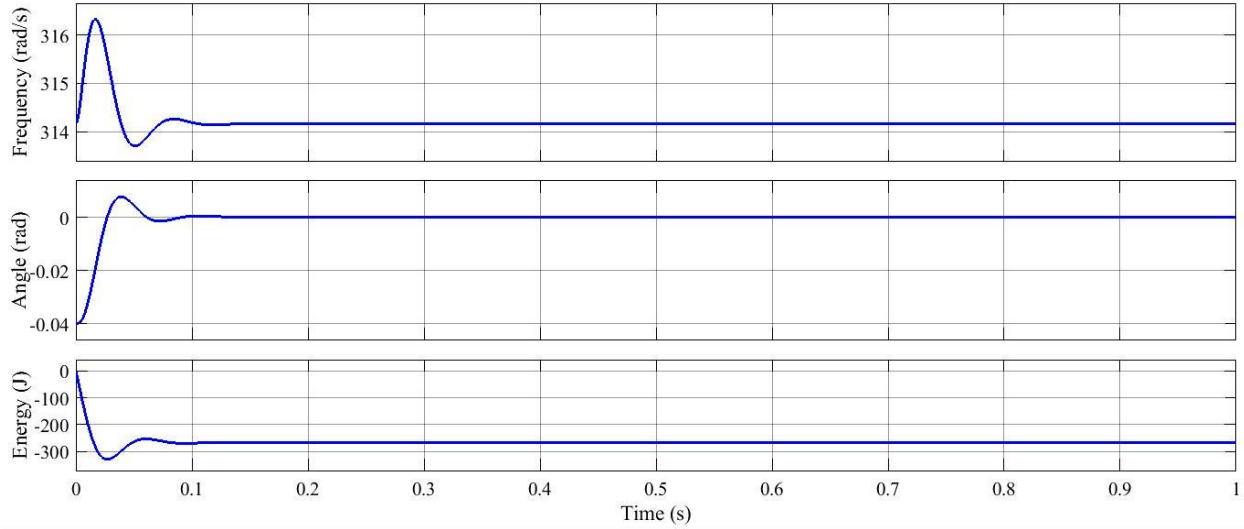

Fig. 6.5. Block diagram of single phase inner loop [30].

49

Fig. 6.6. Inverter (top) frequency (middle) angle and (bottom) energy with Integrated filter.
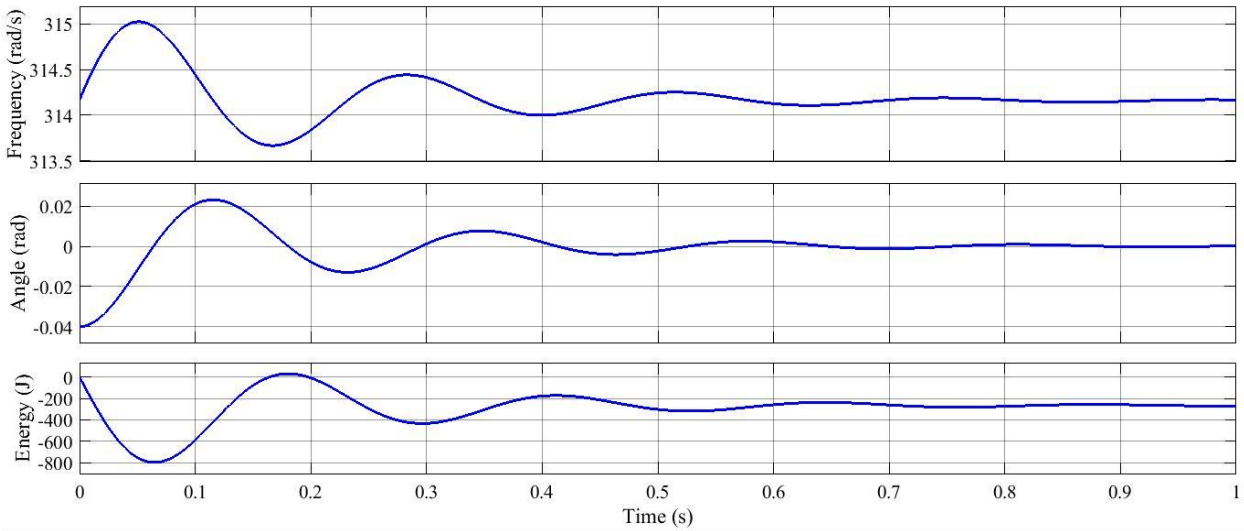

Fig. 6.7. Inverter (top) frequency (middle) angle and (bottom) energy with LP.

6.6   UPS System with Buck Boost Converter Simulation Results

The simulation of Fig. 6.1 was configured using MATLAB/Simulink™. The input voltage is 500 V dc and the grid voltage is 480 V. A buck-boost converter is used to change or discharge the batteries depending on the power flow. A three-phase bidirectional inverter is used

to inverter the voltage from dc to ac during battery charging mode, or from ac to dc when the batteries are discharging their voltage to the grid. Simulation parameters are listed in Table 6.1 [28]. Fig. 6.8 shows the voltage of the boost converter (top), three phase inverter voltage (middle) and the RMS grid voltage (bottom). Detailed MATLAB/Simulink™ is given in Appendix C.2.

Table 6.1. Simulation parameters [28].

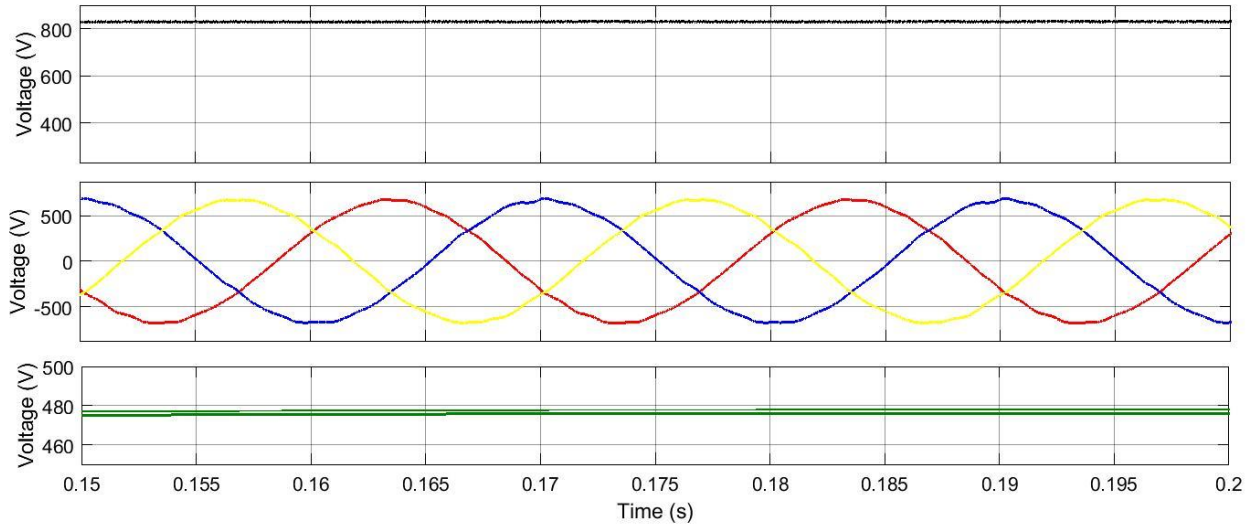| Symbols	Descriptions	Values
L_1	Inverter inductor filter	350 μH
L_2	Grid inductor filter	250 μH
C	Filter capacitor	160 μF
C_{dc}	Dc-link capacitor	2000 μF
P	Active power rating	60 kW
Q	Reactive power rating	45 kVAR

Fig. 6. 8. (top) Inverter output voltage ,(middle) three phase inverter output, (bottom) RMS inverter output.

51

Fig. 6.9 shows the transition from battery charging mode to discharing mode at t=0.5 s. The dc-link capacitor was adjusted by the inverter during the first mode, while the boost converter controlled it after the transition happened. It can be seen that the voltage of the dc-link capacitor during the charging mode is higher than that on discharging mode. During the first mode, it was adjusted by the ac dc inverter. When the transition happened, the capacitor discharged its voltage directly. As is mentioned earier that the refrence voltage of the boost is smaller than the inverter refrence voltage, the boost converter operates. Fig. 6.10 shows the transition from battery charging mode, when the converter operateed as boost and controlled the dc-link capacitor, to discharging mode. This transition is done manually by changing the refrence power.
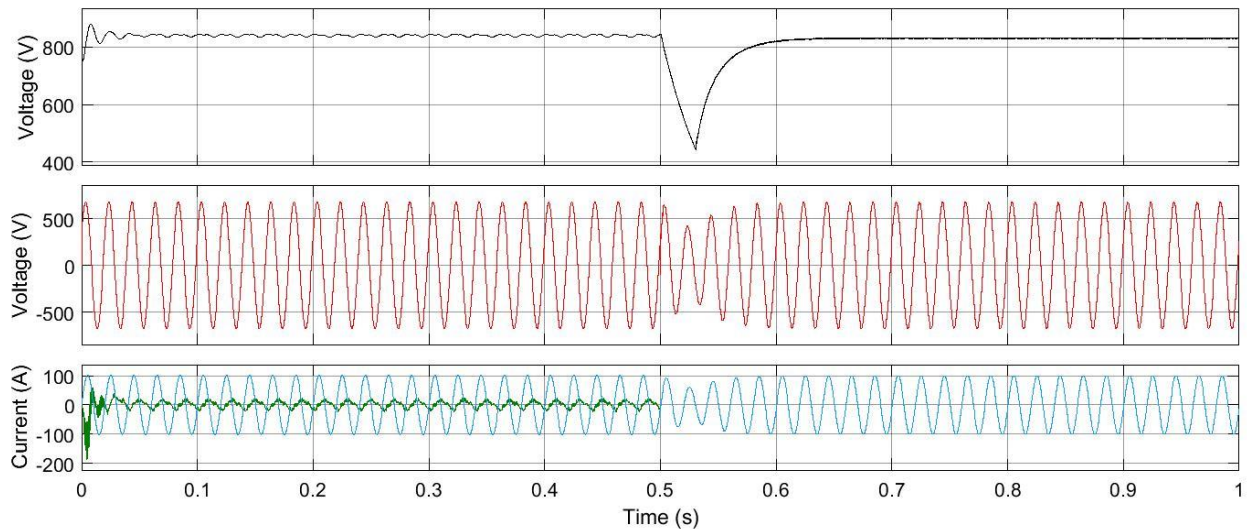

Fig. 6. 9. (top) dc-link capacitor voltage, (middle) load voltage, (bottom) load current(blue) and UPS current (green).
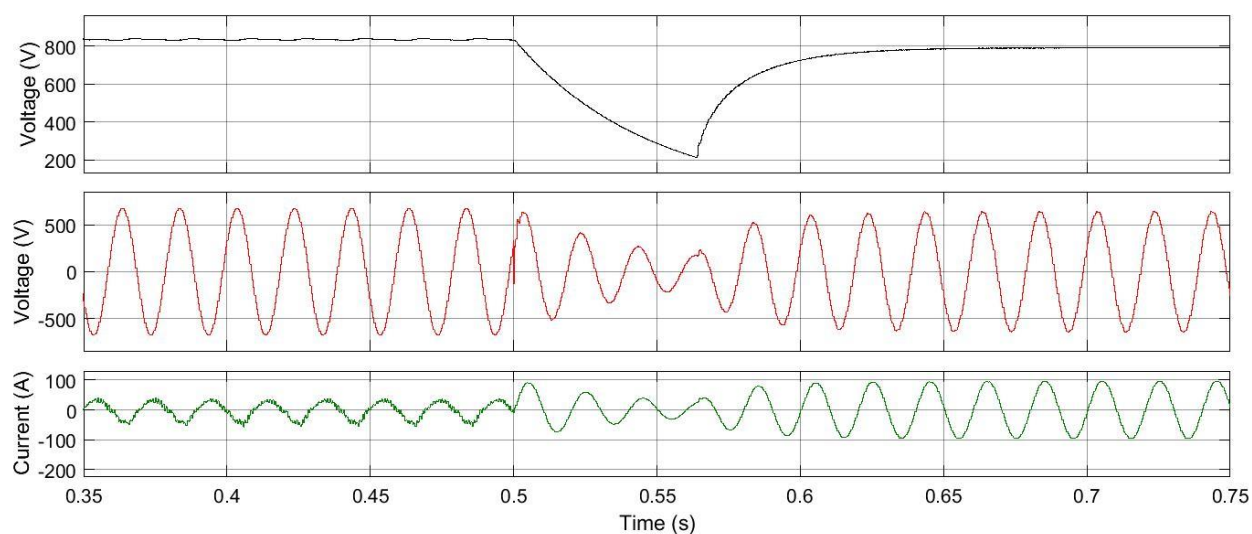
Fig. 6.10. (top) dc-link capacitor voltage, (middle) load voltage, (bottom) UPS current.

6.7   High Step-Up/Down Transformerless MMC for UPS Systems

This section demonstrates the effectiveness in using a high ratio step-up/down (bidirectional) transformerless dc-dc MMC that can be used to interface a battery storage system for grid-tied/islanded microgrid applications.

The benefit of using this type of transformerless MMC converter compared to a conventional buck-boost is that it reduces input voltage level. The previous section was done with a conventional buck-boost converter. As is mentioned earlier, the input voltage from the batteries is 500 V. However, since the proposed transformerless MMC can step up the voltage with 1:10, the input voltage is chosen to be 96 V. Reducing the number of series batteries results in a topology that is flexible for inexpensive microgrid connections.

Fig. 6.11 shows the transition from battery charging mode to discharing mode at t=0.5 s. The dc-link capacitor was adjusted by the inverter during the first mode. The high step-up MMC

53

controls the voltage of the dc-link capacitor after the transition has happened. It can be seen that the voltage of the dc-link capacitor during the charging mode is higher than that on discharging mode. Moreover, the dc-link capacitor voltage using transformerless MMC is higher than the buck-boost converter. As a result, the transformerless MMC provides a high range of voltage at the dc-link capacitor making the controller more accurate and flexible.

A controller for fault monitoring is simulated for safety requirements since this topology is non-isolated. Grid current is monitored and compared with set values (in this case 500Amps which can be changed as per the requirements). When current is higher than the set value and when battery is in discharging mode, then STS will be opened and load power is supplied from the battery to maintain a constant load voltage as shown in Fig 6.12. Three phase fault is created in all the phases at t=0.1 s. MATLAB/Simulink™ implementation of the transformerless MMC for UPS system is presented in Appendix C.3.
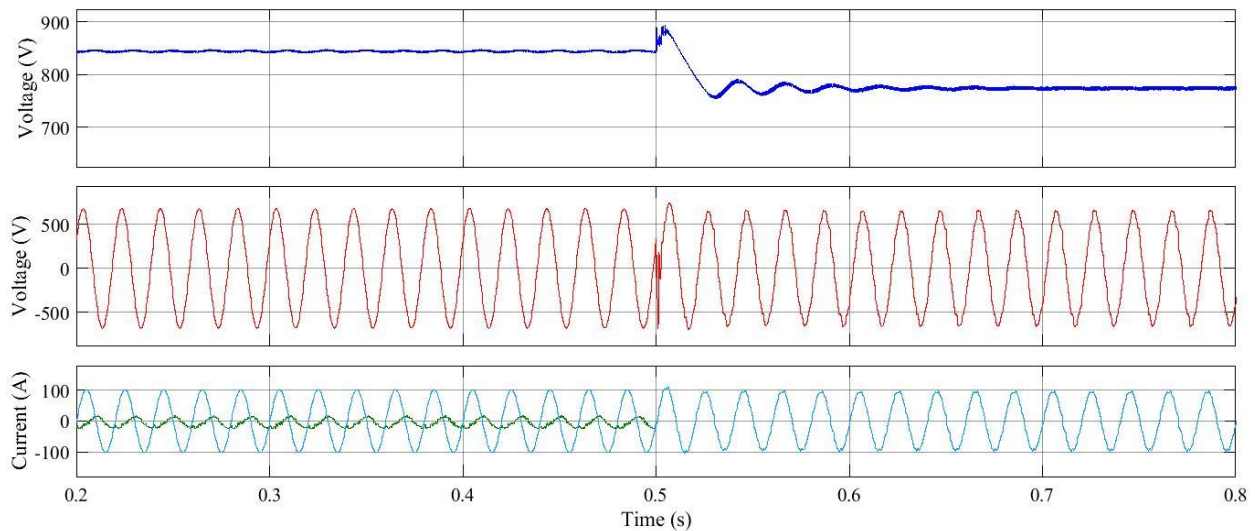

Fig. 6. 11. (top) dc-link capacitor voltage, (middle) load voltage, (bottom) load current(blue) and UPS current (green).
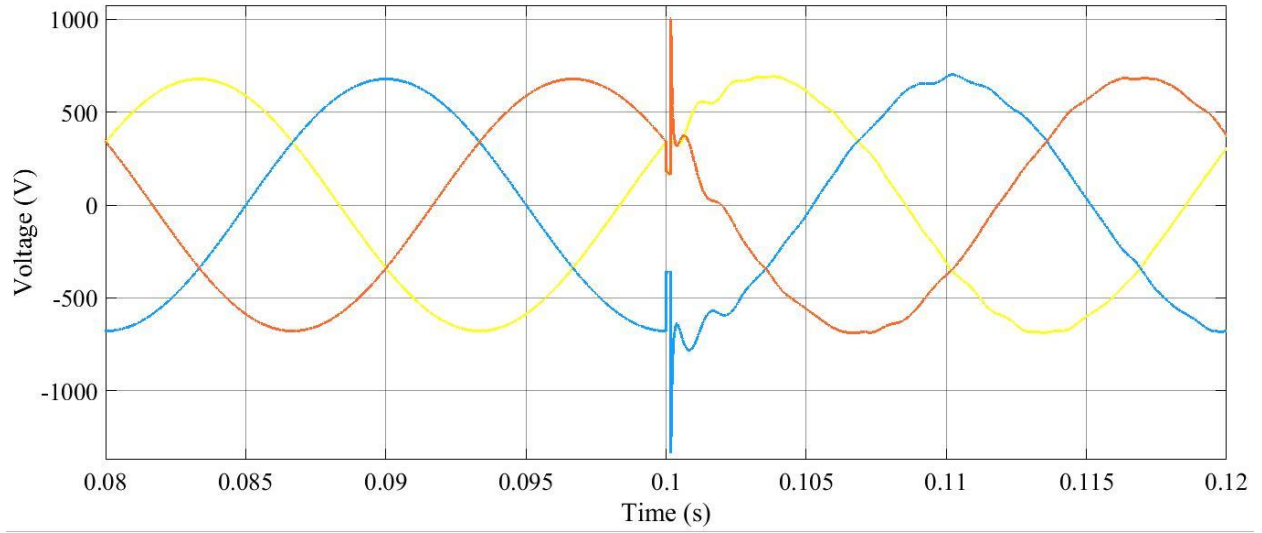
Fig. 6. 12. Load phase voltage when a grid fault occurs at t=0.1s.

CHAPTER SEVEN

CONCLUSIONS AND FUTURE WORK

7.1   Conclusions

This thesis shows the effectiveness in using a new type of high ratio transformerless step-up/down dc-dc modular multilevel converter. It shows the possibility of multilevel converters in providing low-voltage renewable energy sources to a medium voltage dc grid. Detailed MATLAB-Simulink simulations showed the ability of the proposed converter under medium voltage conditions. Upon simulation and examination of the results, it is clear that dc-dc multilevel converters are becoming more capable of interfacing to the dc grid without the need of a transformer. This research shows that interfacing low voltage renewable energy sources with the power grid is not only desirable, but achievable and realistic.

Recent updates to IEC standard 62109, UL 1741 and the National Electric Code include standards for using non-isolated converters. The converter meets these standards and is very responsive to ground faults. The MMC demonstrates a very fast response to a change in the power flow condition. The output voltage ripple is also less than 1 percent. Additionally, it provides power grid isolation and helps solve the low-voltage to medium-voltage problem without a transformer. The absence of the transformer makes this circuit more cost-effective. Not only does the system have a high step-up/down voltage conversion ratio, but it is also bidirectional in power flow. It was shown how this converter compares to other medium-voltage dc-dc topologies and how effective this MMC is with isolation and performance during fault conditions.

7.2   Future Work

There are a number of further activities that could be explored for further developing the converter circuit described by this research. These are identified as the following:

- A state-space model for transient analysis and direct power control could be developed.

- Design of a controller and observer for the proposed topology for reducing the number of sensors required for closed-loop control.

- A small-scale prototype could be built for a medium voltage (3000 V) system.

References

[1]   M. Sahoo and K. S. Kumar, "High gain step up DC-DC converter for DC micro-grid application," *Information and Automation for Sustainability (ICIAfS), 2014 7th International Conference on*, Colombo, 2014, pp. 1-5.

[2]   T. J. Liang and J. H. Lee, "Novel High-Conversion-Ratio High-Efficiency Isolated Bidirectional DC–DC Converter," in *IEEE Transactions on Industrial Electronics*, vol. 62, no. 7, pp. 4492-4503, July 2015.

[3]   C. c. Lin, L. s. Yang and G. W. Wu, "Study of a non-isolated bidirectional DC-DC converter," in *IET Power Electronics*, vol. 6, no. 1, pp. 30-37, Jan. 2013.

[4]   W. Li, J. Liu, J. Wu and X. He, "Design and Analysis of Isolated ZVT Boost Converters for High-Efficiency and High-Step-Up Applications," in *IEEE Transactions on Power Electronics*, vol. 22, no. 6, pp. 2363-2374, Nov. 2007.

[5]   M. Sahoo and K. S. Kumar, "High gain step up DC-DC converter for DC micro-grid application," *Information and Automation for Sustainability (ICIAfS), 2014 7th International Conference on*, Colombo, 2014, pp. 1-5.

[6]   L. w. Zhou, B. x. Zhu, Q. m. Luo and S. Chen, "Interleaved non-isolated high step-up DC/DC converter based on the diode-capacitor multiplier," in *IET Power Electronics*, vol. 7, no. 2, pp. 390-397, February 2014.

[7]   M. S. Bhaskar, N. SreeramulaReddy, R. K. P. Kumar and Y. B. S. S. Gupta, "A novel high step-up DC-DC multilevel buck-boost converter using voltage-lift switched-inductor cell," *Computer Communication and Systems, 2014 International Conference on*, Chennai, 2014, pp. 271-275.

[8]   S. Choi, V. G. Agelidis, J. Yang, D. Coutellier and P. Marabeas, "Analysis, design and experimental results of a floating-output interleaved-input boost-derived DC-DC high-gain transformer-less converter," in *IET Power Electronics*, vol. 4, no. 1, pp. 168-180, January 2011.

[9]   H. Athab, A. Yazdani and Bin Wu, "A transformer-Less DC-DC converter with large voltage transformation ratio for medium-voltage DC grid applications," *Power and Energy Society General Meeting (PES), 2013 IEEE*, Vancouver, BC, 2013, pp. 1-5.

[10]   N. Denniston, A. M. Massoud, S. Ahmed and P. N. Enjeti, "Multiple-Module High-Gain High-Voltage DC–DC Transformers for Offshore Wind Energy Systems," in *IEEE Transactions on Industrial Electronics*, vol. 58, no. 5, pp. 1877-1886, May 2011.

[11]   L. Zuñiga-Garcia, A. Zaragoza-Hernández, J. M. Nadal-Martínez, G. A. Anaya-Ruiz, E. L. Moreno-Goytia, L. E. Ugalde-Caballero, and V. Venegas-Rebollar, "MMC technology and its participation in the integration of variable renewable energies and implementation of DC grids," *Power, Electronics and Computing (ROPEC), 2014 IEEE International Autumn Meeting on*, Ixtapa, 2014, pp. 1-6.

[12]   S. Debnath, J. Qin, B. Bahrani, M. Saeedifard and P. Barbosa, "Operation, Control, and Applications of the Modular Multilevel Converter: A Review," in *IEEE Transactions on Power Electronics*, vol. 30, no. 1, pp. 37-53, Jan. 2015.

[13]   A. K. Sahoo, R. Otero-De-Leon and N. Mohan, "Review of modular multilevel converters for teaching a graduate-level course of power electronics in power systems," *North American Power Symposium (NAPS), 2013*, Manhattan, KS, 2013, pp. 1-6.

[14]   M. A. Perez, S. Bernet, J. Rodriguez, S. Kouro and R. Lizana, "Circuit Topologies, Modeling, Control Schemes, and Applications of Modular Multilevel Converters," in *IEEE Transactions on Power Electronics*, vol. 30, no. 1, pp. 4-17, Jan. 2015.

[15]   J. Wang, R. Burgos and D. Boroyevich, "A survey on the modular multilevel converters — Modeling, modulation and controls," *in IEEE Energy Conversion Congress and Exposition*, Denver, CO, 2013, pp. 3984-3991.

[16]   S. Debnath and M. Saeedifard, "Simulation-Based Gradient-Descent Optimization of Modular Multilevel Converter Controller Parameters," in *IEEE Transactions on Industrial Electronics*, vol. 63, no. 1, pp. 102-112, Jan. 2016..

[17]   F. Deng and Z. Chen, "Voltage-Balancing Method for Modular Multilevel Converters Switched at Grid Frequency," in *IEEE Transactions on Industrial Electronics*, vol. 62, no. 5, pp. 2835-2847, May 2015.

[18]   H. Wang, J. Cao, Z. He, J. Yang, Z. Han and G. Chen, "Research on Overvoltage for XLPE Cable in a Modular Multilevel Converter HVDC Transmission System," in *IEEE Transactions on Power Delivery*, vol. 31, no. 2, pp. 683-692, April 2016.

[19]   X. Zhang and T. C. Green, "The new family of high step ratio modular multilevel DC-DC converters," *Applied Power Electronics Conference and Exposition (APEC), 2015 IEEE*, Charlotte, NC, 2015, pp. 1743-1750.

[20]   X. Zhang and T. C. Green, "The Modular Multilevel Converter for High Step-Up Ratio DC–DC Conversion," in *IEEE Transactions on Industrial Electronics*, vol. 62, no. 8, pp. 4925-4936, Aug. 2015.

[21]   L. A. Garcia Rodriguez, E. Williams, J. Carlos Balda and C. Stewart, "A comparison of selected silicon and silicon-carbide switching devices for PV microinverter applications,"*2013 4th IEEE International Symposium on Power Electronics for Distributed Generation Systems (PEDG)*, Rogers, AR, 2013, pp. 1-7.

[22]   EPIA, "Global market outlook for photovoltaics 2014–2018," *EPIA Report*, 2014. [Online]. Available: http://www.epia.org/news/publications/ global-market-outlook-for-photovoltaics-2014 2018/

[23]   J. Echeverría, S. Kouro, M. Pérez and H. Abu-rub, "Multi-modular cascaded DC-DC converter for HVDC grid connection of large-scale photovoltaic power systems," *Industrial Electronics Society, IECON 2013 - 39th Annual Conference of the IEEE*, Vienna, 2013, pp. 6999-7005.

[24]   J. Fisher and D. Brealey, "SolarPro Magazine," *Ungrounded PV Power Systems in the NEC: Page 3 of 12*. [Online]. Available at: https://solarprofessional.com/articles/design-installation/ungrounded-pv-power-systems-in-the-nec/page/0/2. [Accessed: 18-Apr-2016].

[25]   O. Lopez, R. Teodorescu, F. Freijedo and J. Doval-Gandoy, "Eliminating ground current in a transformerless photovoltaic application," *Power Engineering Society General Meeting, 2007. IEEE*, Tampa, FL, 2007, pp. 1-5.

[26]   T. Kerekes, "Analysis and modeling of transformerless photovoltaic inverter systems," thesis, 2009.

[27]   M. Calais and V. G. Agelidis, "Multilevel converters for single-phase grid connected photovoltaic systems-an overview," *Industrial Electronics, 1998. Proceedings. ISIE '98. IEEE International Symposium on*, Pretoria, 1998, pp. 224-229.

[28]   M. A. Abusara, J. M. Guerrero and S. M. Sharkh, "Line-Interactive UPS for Microgrids," in *IEEE Transactions on Industrial Electronics*, vol. 61, no. 3, pp. 1292-1300, March 2014.

[29]   S. M. Sharkh; M. A. Abu-Sara; G. I. Orfanoudakis; B. Hussain, "Line Interactive UPS," in *Power Electronic Converters for Microgrids* , 1, Wiley-IEEE Press, 2014, pp.352-doi: 10.1002/9780470824054.ch9

[30]   M. A. Abusara, S. M. Sharkh, and J. M. Guerrero, "Improved droop control strategy for grid-connected inverters," *Sustainable Energy, Grids and Networks*, vol. 1, pp. 10–19, 2015.

[31]   M. A. Abusara and S. M. Sharkh, "Control of line interactive UPS systems in a Microgrid," *Industrial Electronics (ISIE), 2011 IEEE International Symposium on*, Gdansk, 2011, pp. 1433-1440.

[32]   J. M. Guerrero, J. C. Vasquez, J. Matas, M. Castilla and L. Garcia de Vicuna, "Control Strategy for Flexible Microgrid Based on Parallel Line-Interactive UPS Systems," in *IEEE Transactions on Industrial Electronics*, vol. 56, no. 3, pp. 726-736, March 2009.

[33]   X. Zhang, H. Zhang, J. M. Guerrero and X. Ma, "Reactive power compensation for parallel inverters without control interconnections in microgrid," *Industrial Electronics, 2008. IECON 2008. 34th Annual Conference of IEEE*, Orlando, FL, 2008, pp. 922-925.

[34]   J. M. Guerrero, L. G. de Vicuna, J. Matas, J. Miret and M. Castilla, "A high-performance DSP-controller for parallel operation of online UPS systems," *Applied Power Electronics Conference and Exposition, 2004. APEC '04. Nineteenth Annual IEEE*, 2004, pp. 463-469 Vol.1.

[35]   E. Planas, A. Gil-de-Muro, J. Andreu, I. Kortabarria and I. M. de Alegría, "Stability analysis and design of droop control method in dq frame for connection in parallel of distributed energy resources," *IECON 2012 - 38th Annual Conference on IEEE Industrial Electronics Society*, Montreal, QC, 2012, pp. 5683-5688.

APPENDIX A.1

MATLAB/SIMULINK™ SIMULATION SETUP FOR HIGH STEP-UP TRANSFORMERLESS MMC

The MATLAB/Simulink™ models that used in Chapter Two to simulate the high step-up MMC are represented in this appendix.
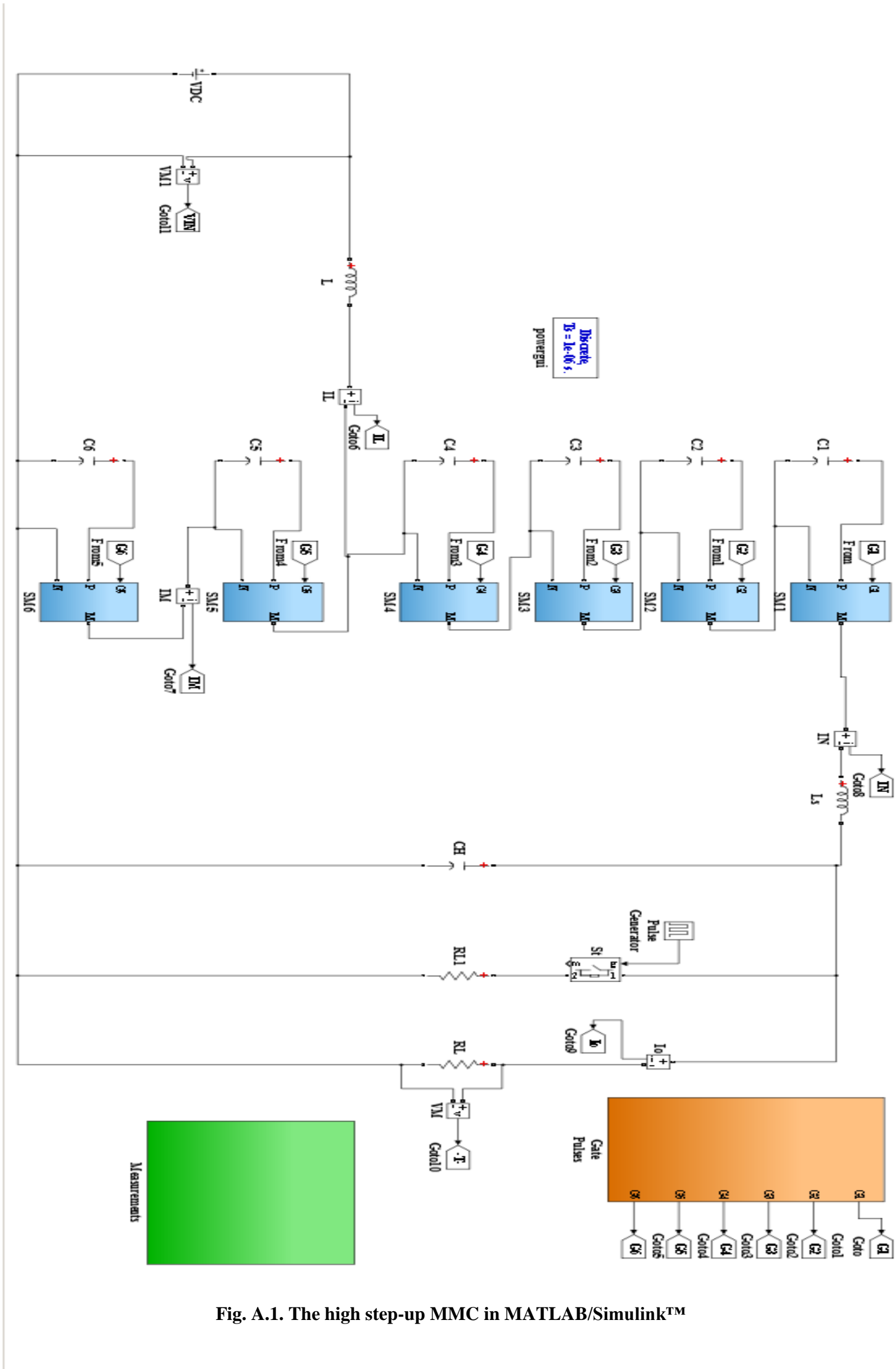
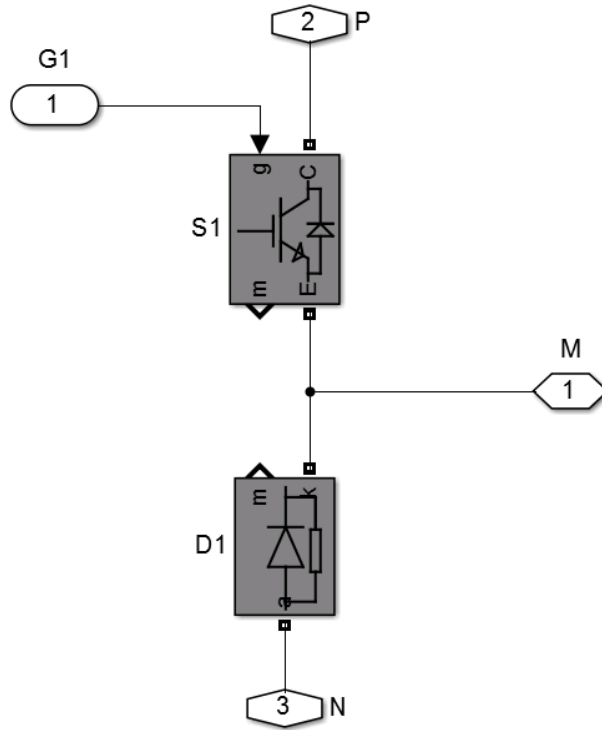**Fig. A.1. The high step-up MMC in MATLAB/Simulink™**

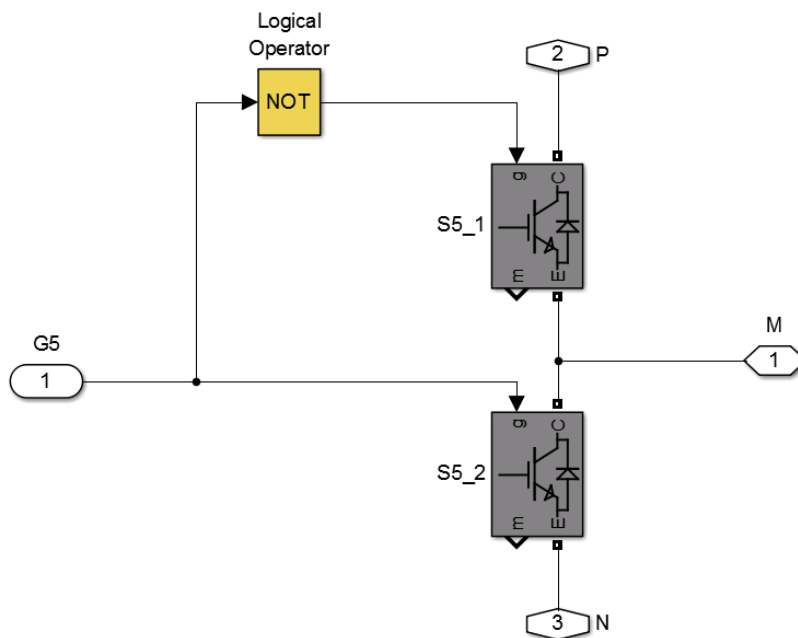**Fig. A.2. An upper submodules implementation in MATLAB/Simulink™**

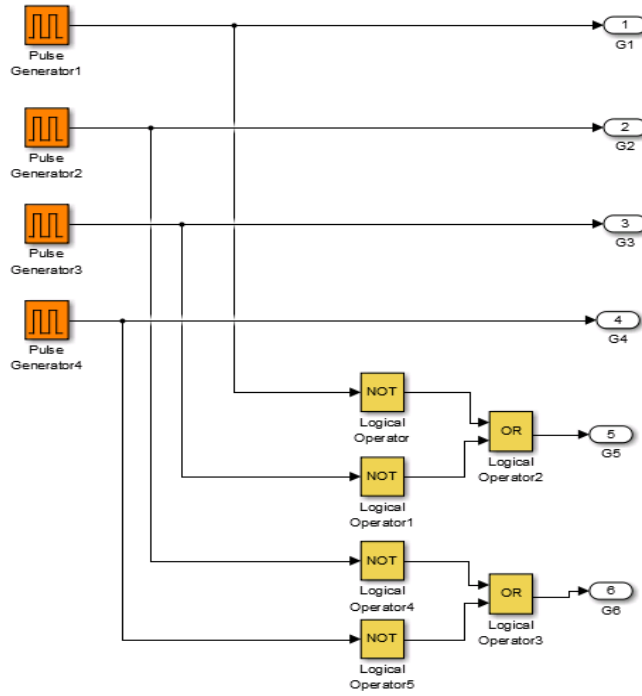**Fig. A.3. A lower submodule implementation in MATLAB/Simulink™**

Fig. A.4. PWM generators in MATLAB/Simulink™

APPENDIX A.2

LTspice SIMULATION SETUP FOR HIGH STEP-UP TRANSFORMERLESS MMC

LTspice simulation models for high step-up transformerless MMC are presented in this appendix.
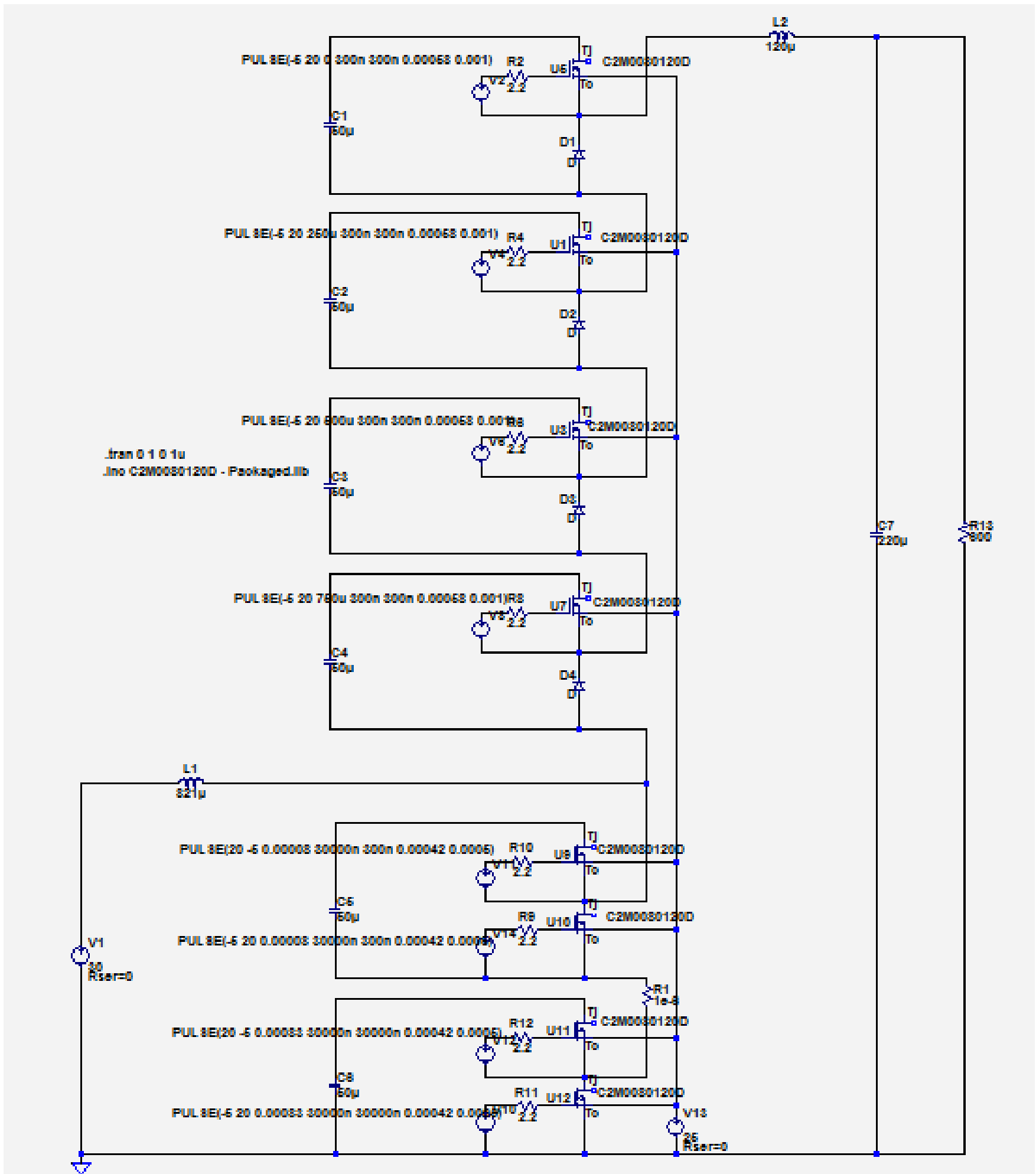
Fig. A.5. A high step-up MMC in LTspice.
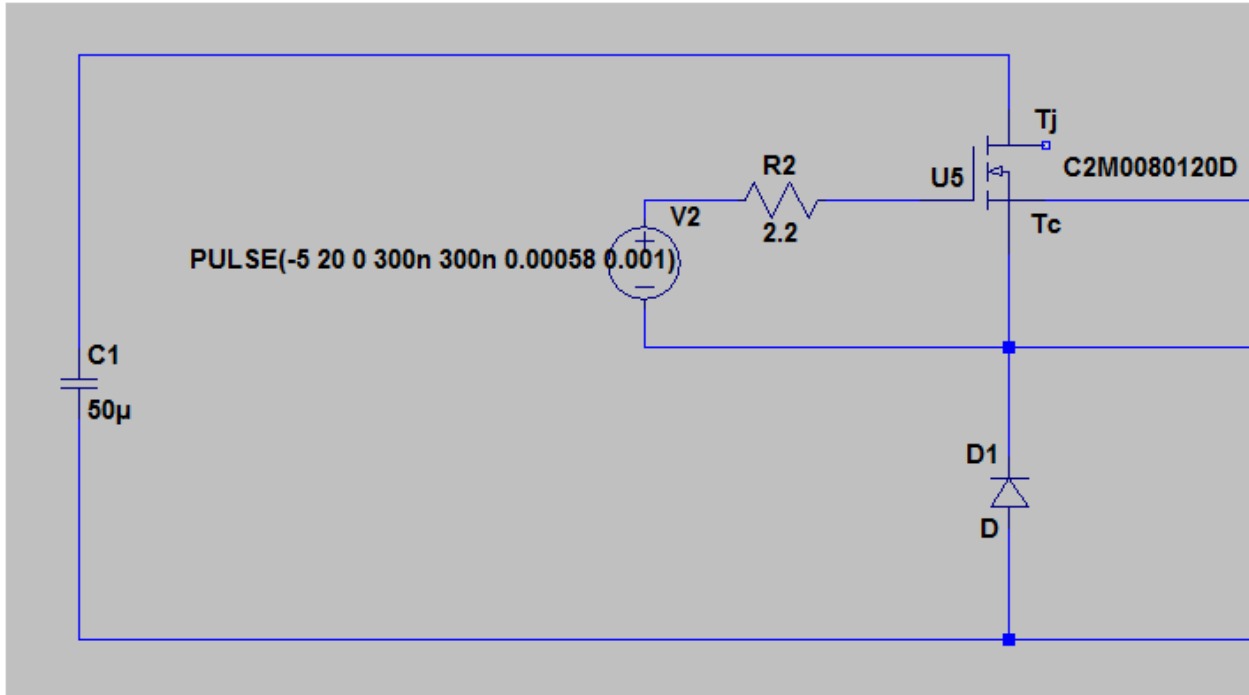
Fig. A.5. An upper submodule implementation in LTspice
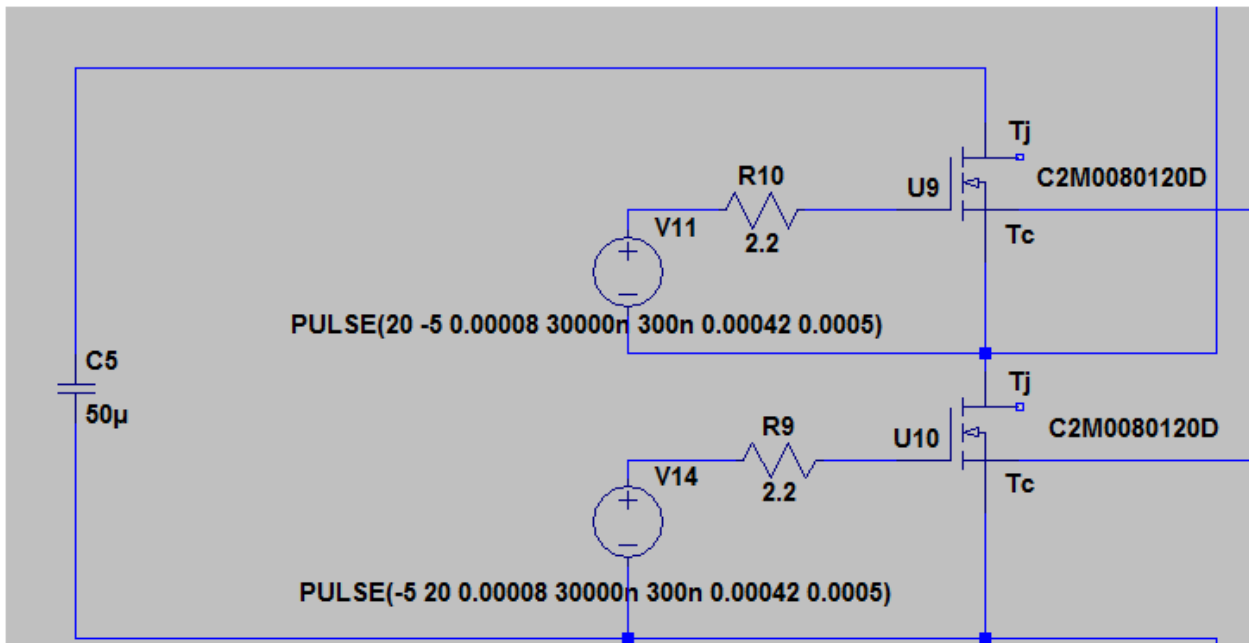
Fig. A.6. A lower submodule implementation in LTspice

66

APPENDIX A.3

MATLAB/SIMULINK™ SIMULATION SETUP FOR HIGH STEP-UP/DOWN TRANSFORMERLESS MMC

MATLAB/SIMULINK™ simulation models for high step-up/down (bidirectional) transformerless MMC are presented in this appendix.
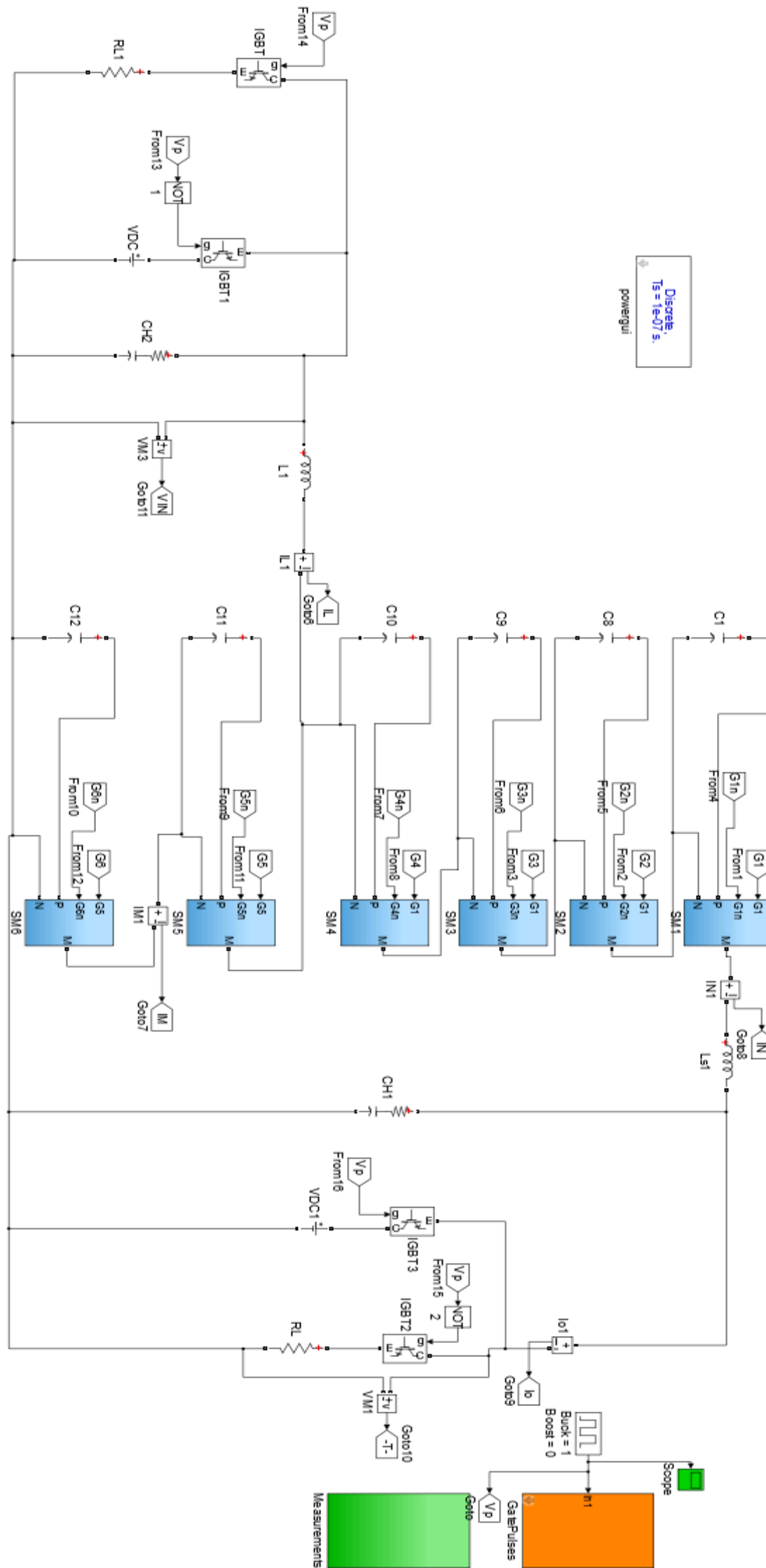
Fig. A.7. The high step-up/down MMC in MATLAB/Simulink™
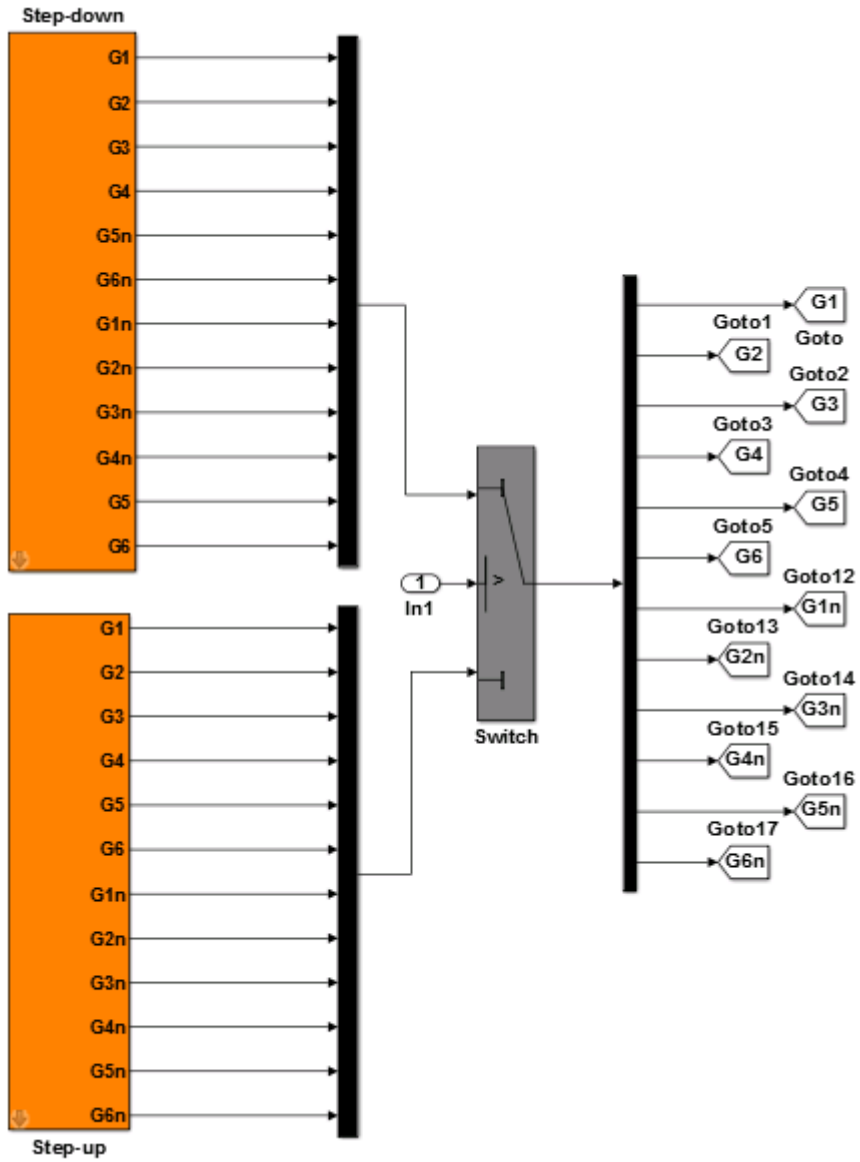
Fig. A.8. PWM for step-up/down MMC in MATLAB/Simulink™

APPENDIX B

MATLAB/SIMULINK™ SIMULATION SETUP FOR CLOSED LOOP CONTROLLER

MATLAB/SIMULINK™ simulation models for closed loop high step-up transformerless MMC are presented in this appendix.
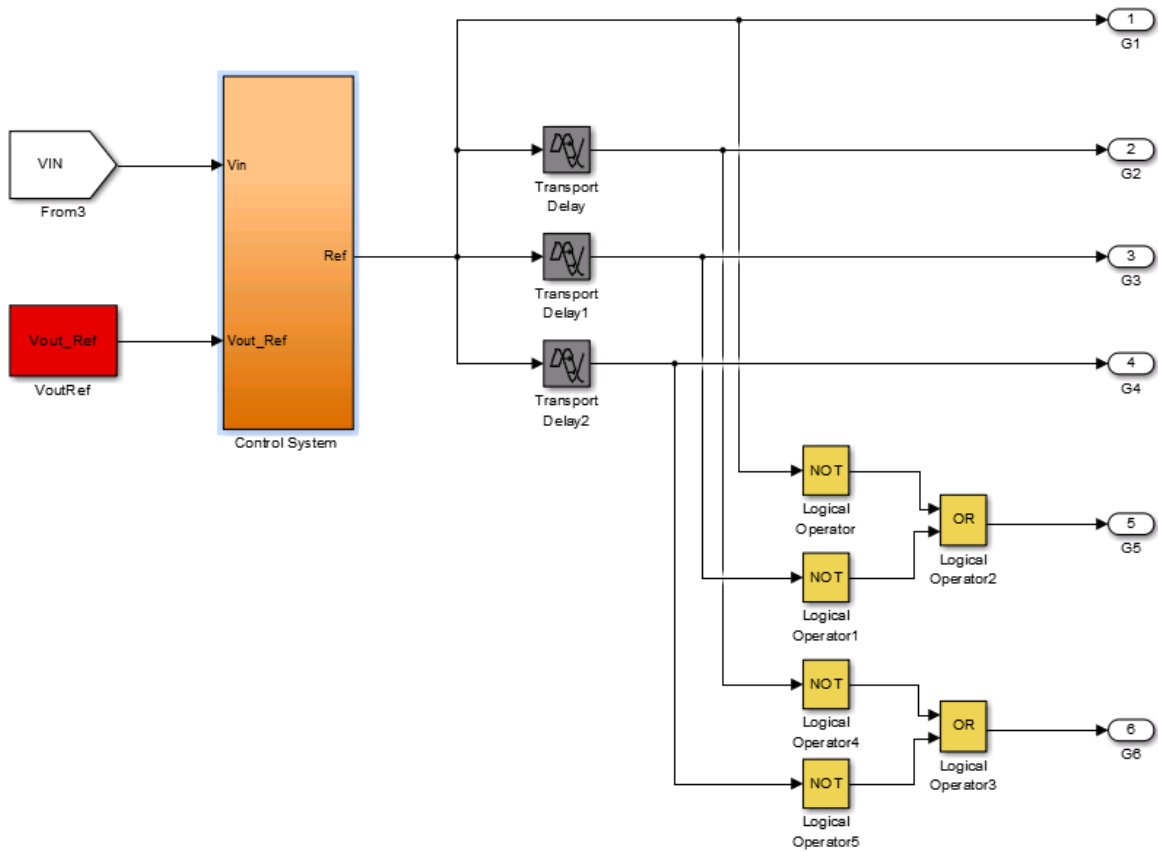
Fig. B.1. Closed loop PWM for step-up MMC in MATLAB/Simulink™
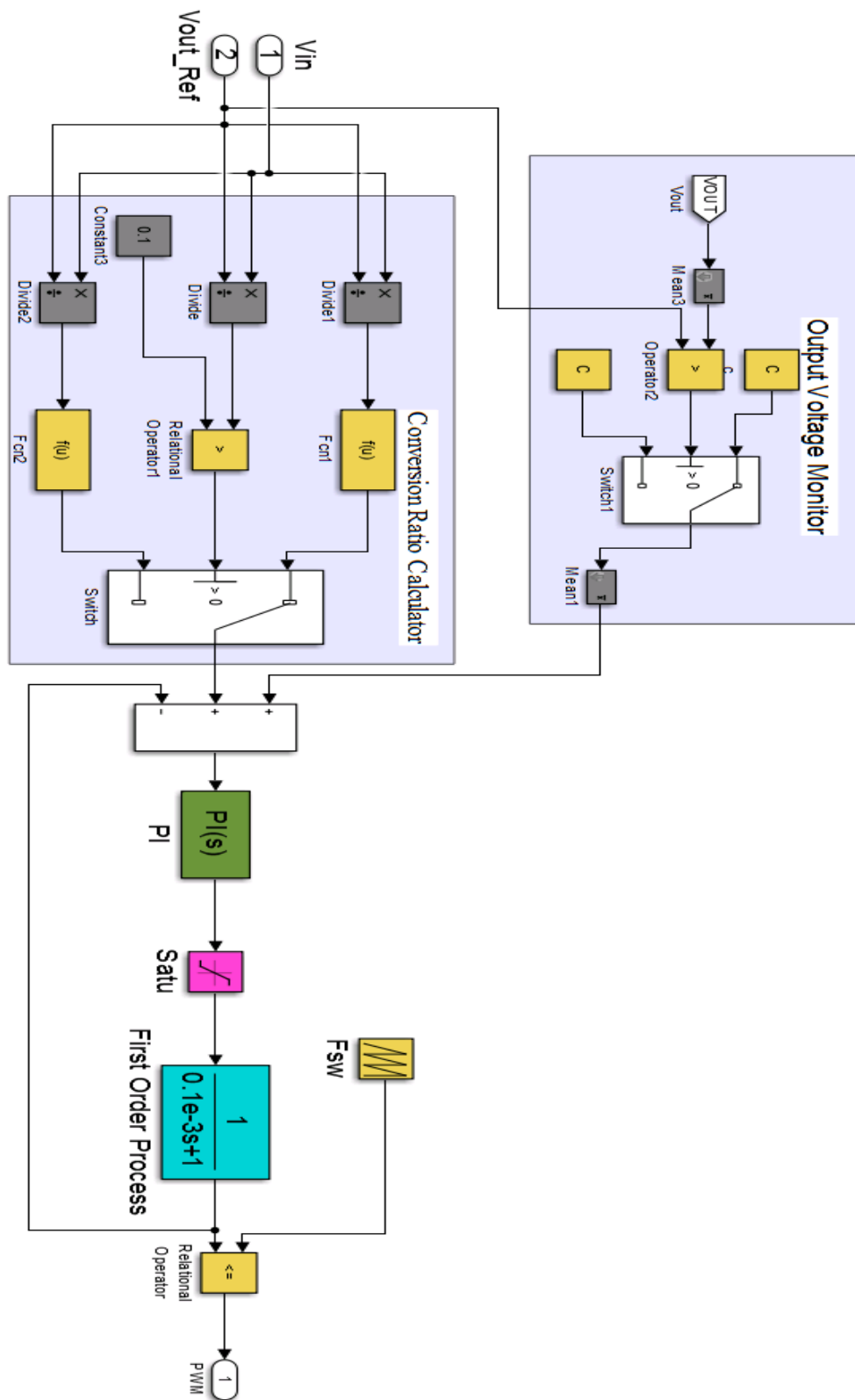
Fig. B.2. Closed loop controller for photovoltaic systems in MATLAB/Simulink™

70

MATLAB/SIMULINK™ SIMULATION FOR SMALL SIGNAL ANALYSIS

The MATLAB/Simulink™ models that used in Chapter Five to simulate the small signal model are in this appendix.
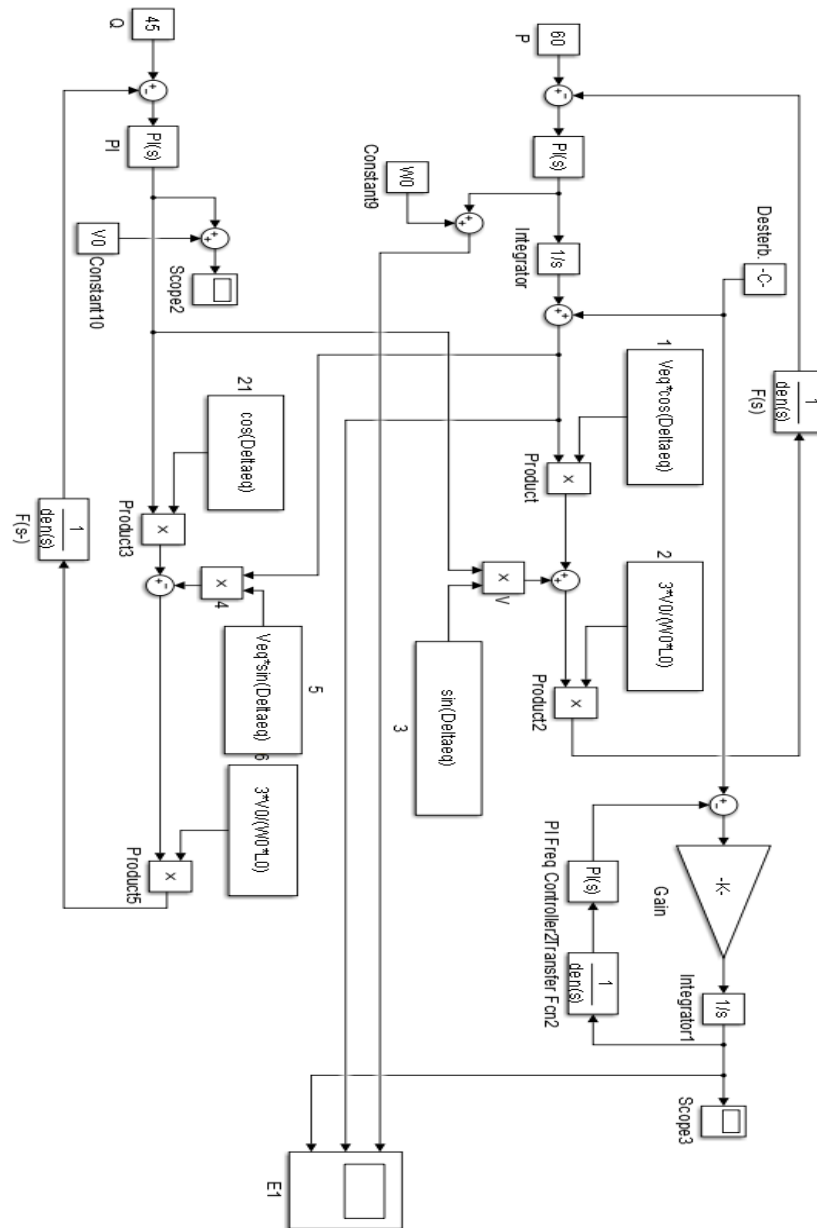
Fig. C.1. Small signal implementation by MATLAB

APPENDIX C.2

MATLAB/SIMULINK™ SIMULATION SETUP FOR UPS WITH BUCK BOOST CONVERTER

The MATLAB/Simulink™ models that used in Chapter Five to simulate the UPSsystem with buck boost converter are in this appendix.
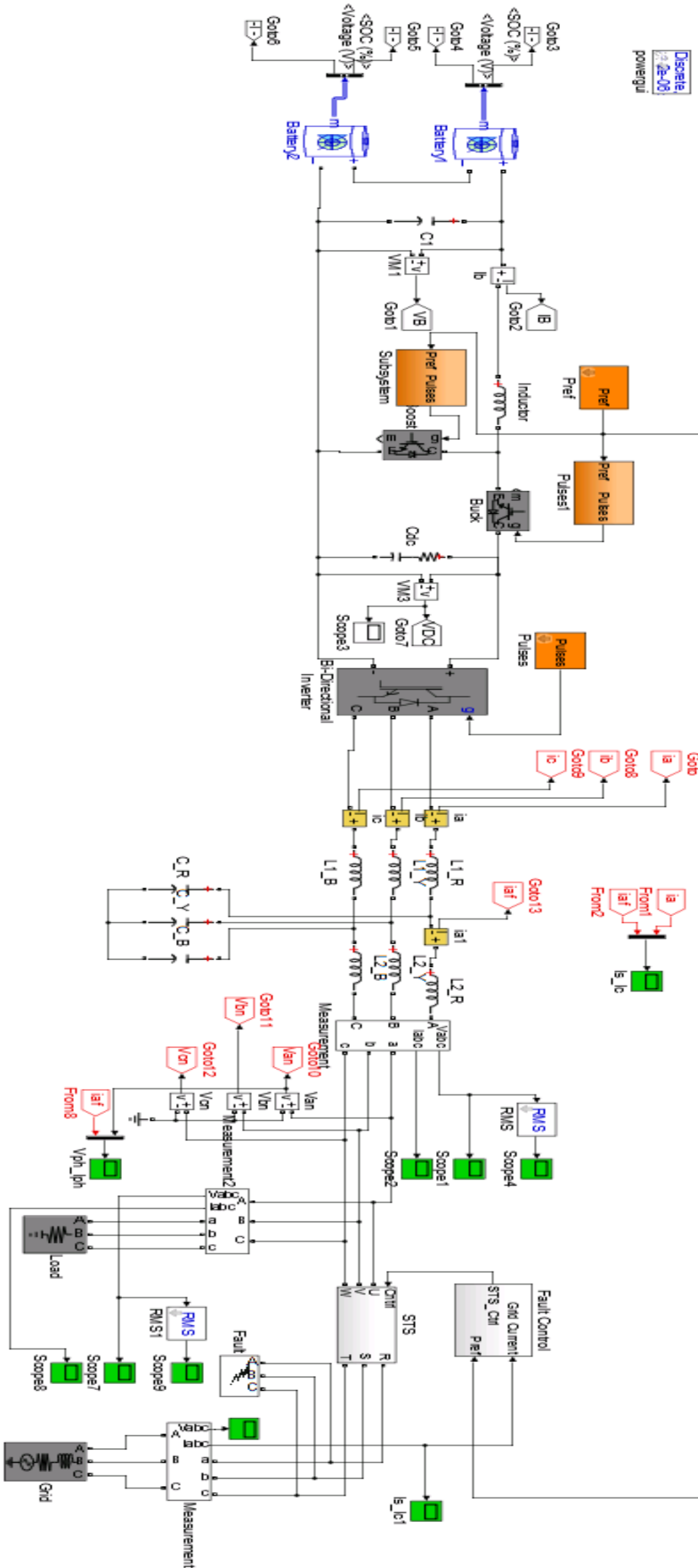
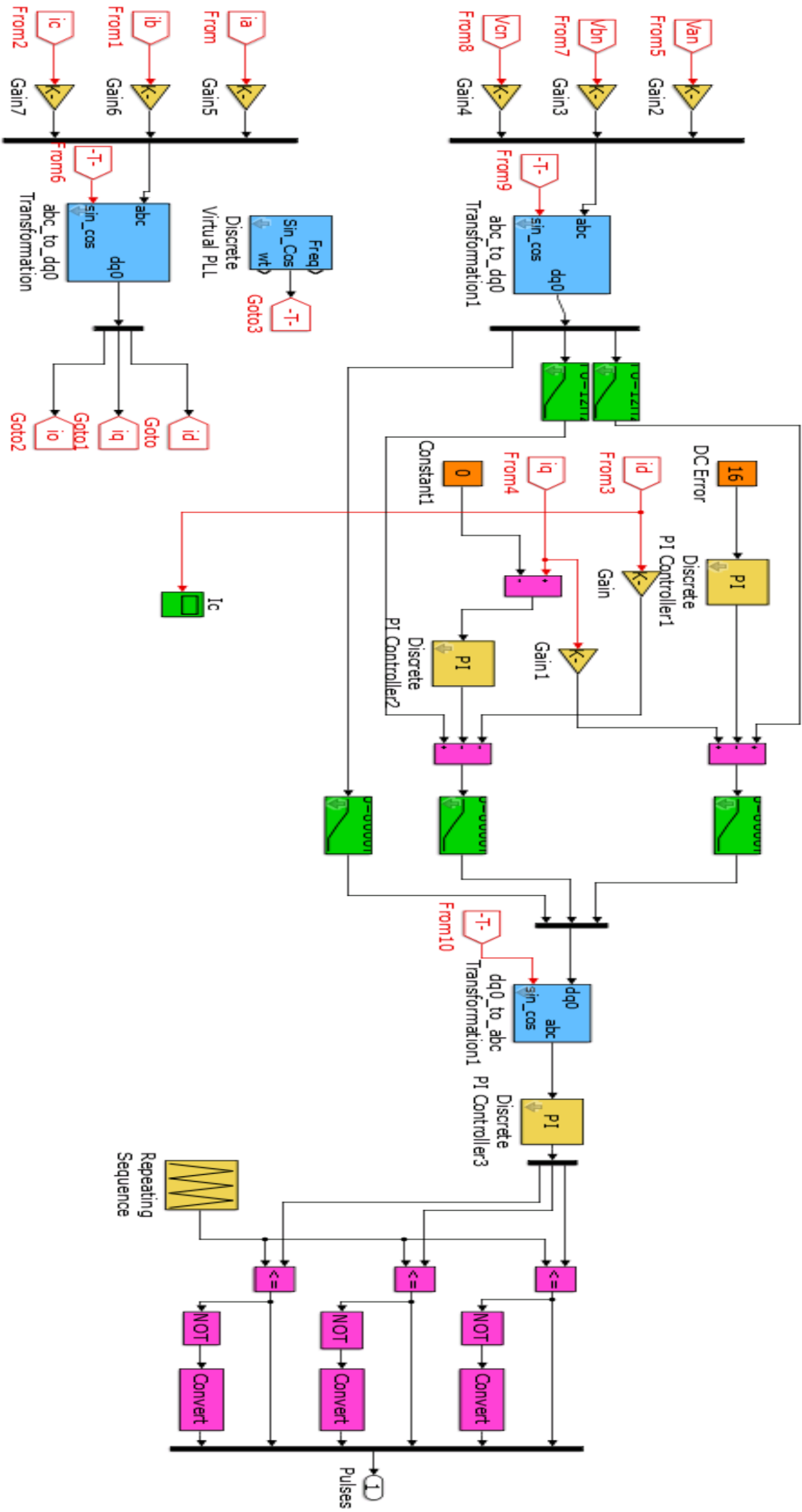**Fig. C. 2. UPS system with buck boost converter in MATLAB/Simulink™**

Fig. C. 3.Three-Phase Inverter controller in Battery charging mode:

APPENDIX C.3

MATLAB/SIMULINK™ SIMULATION SETUP FOR UPS WITH HIGH STEP-UP TRANSFORMERLESS MMC

The MATLAB/Simulink™ models that used in Chapter Five to simulate the transformerless MMC for UPSsystems are in this appendix.
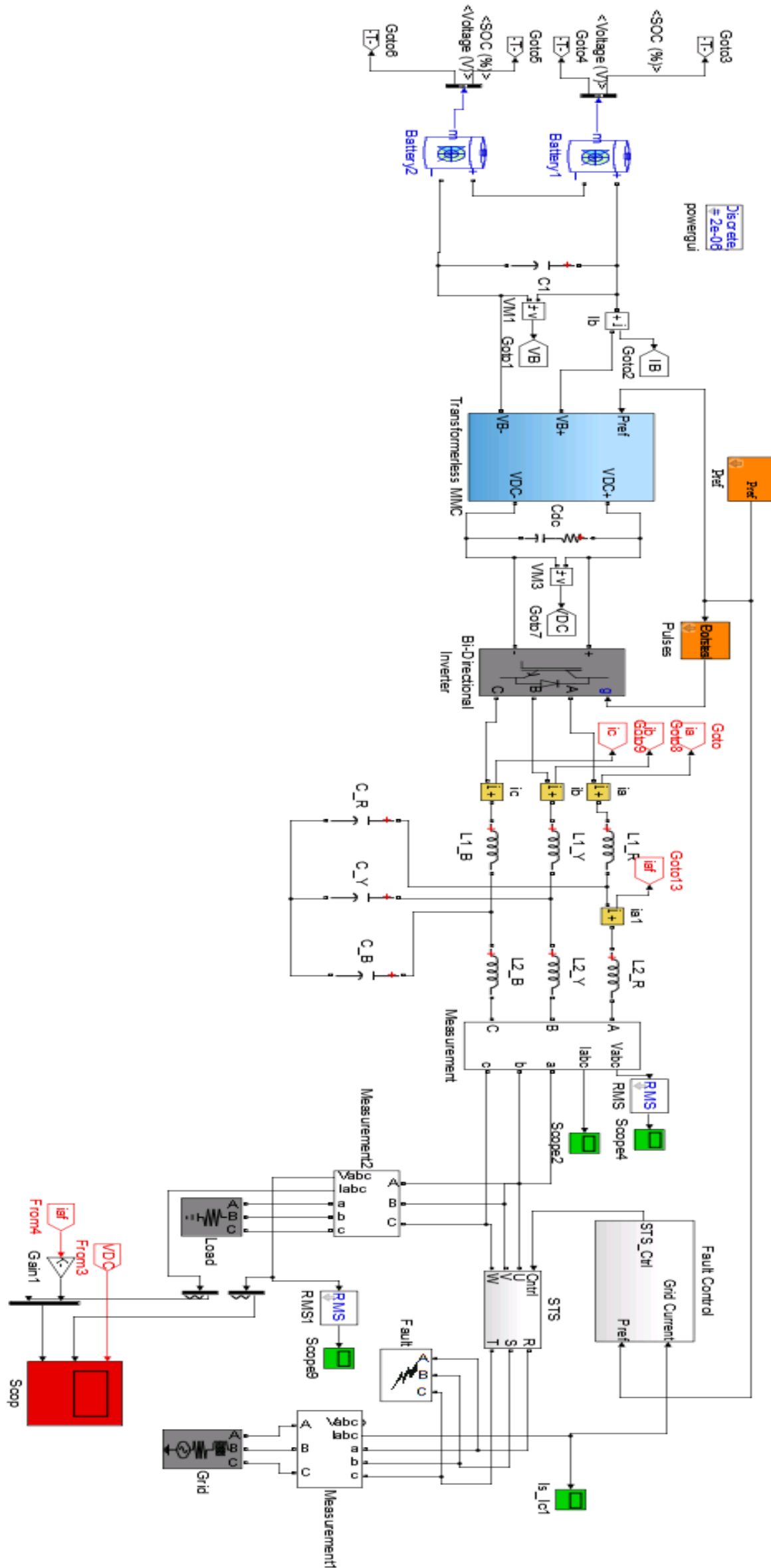

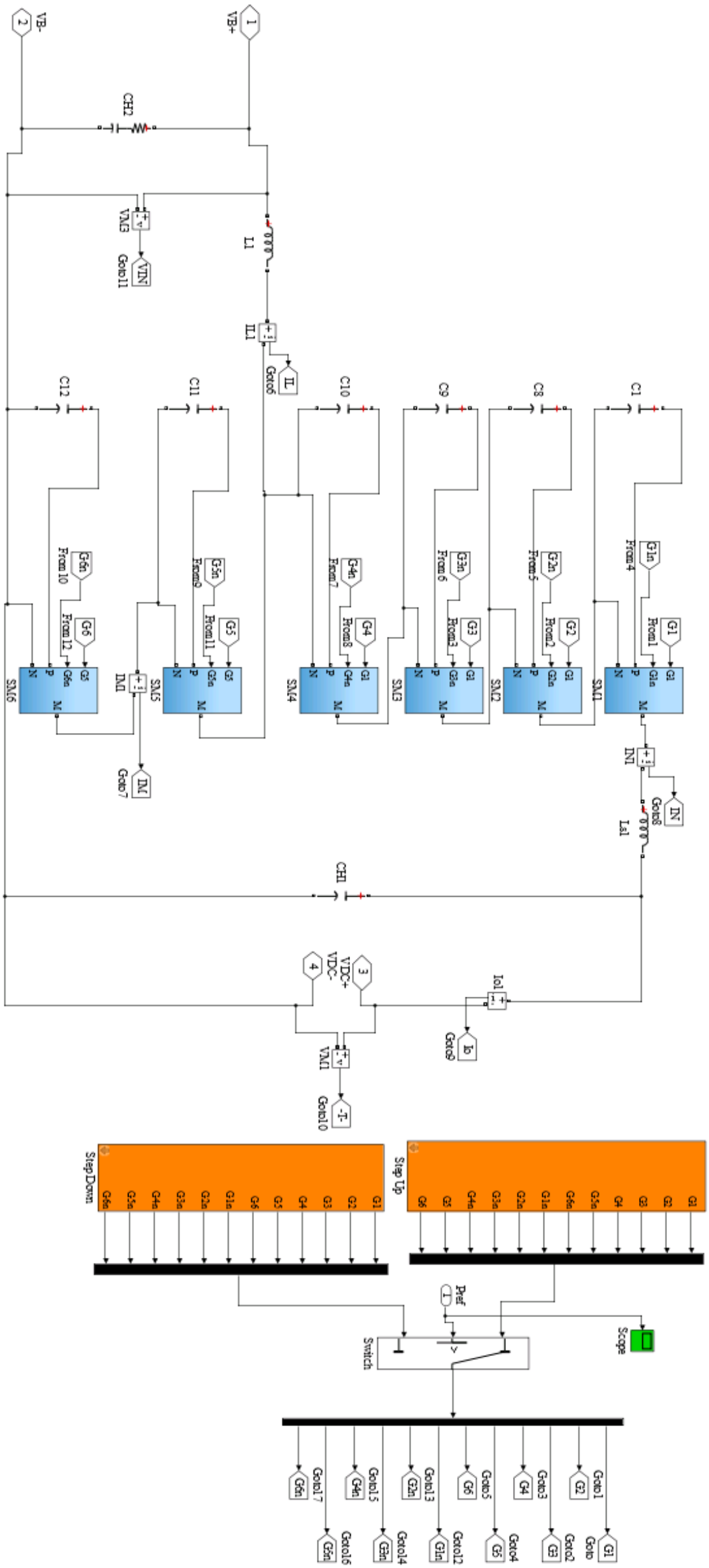**Fig. C. 4. UPS system with transformerless MMC in MATLAB/Simulink™**
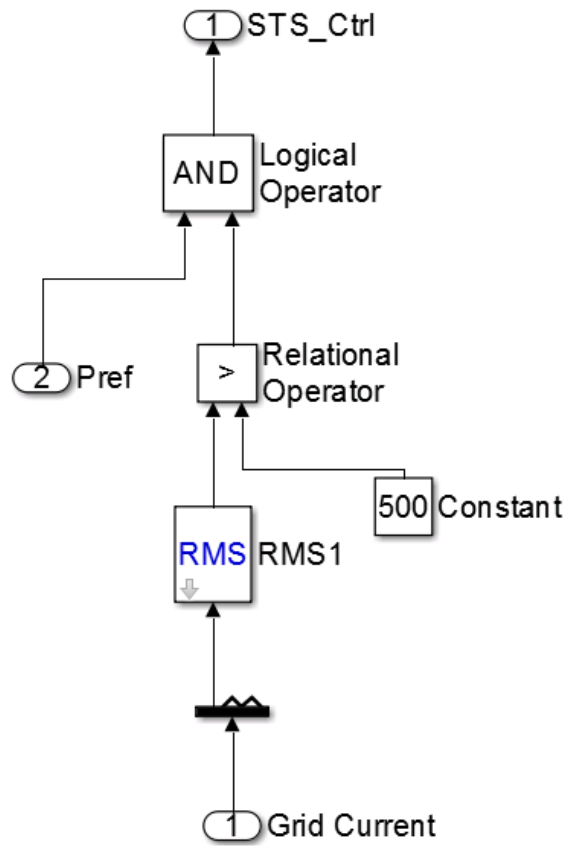
Fig. C. 5. UPS system with transformerless MMC in MATLAB/Simulink™

Fig. C. 6. Fault controller